Linköping Studies in Science and Technology
Dissertation No. 2057

Quantitative Muscle Composition Analysis Using Magnetic Resonance Imaging

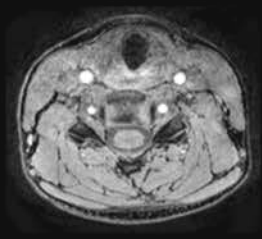

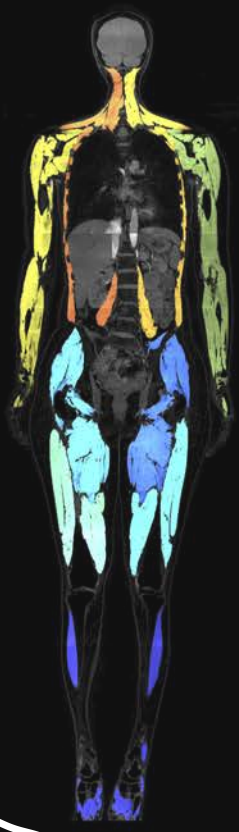

Anette Karlsson

LINKÖPING UNIVERSITY

Linköping Studies in Science and Technology
Dissertations, No. 2057

Quantitative Muscle Composition Analysis Using Magnetic Resonance Imaging

Anette Karlsson

Linköping University
Department of Biomedical Engineering
Division of Biomedical Engineering
SE-581 83 Linköping, Sweden

Linköping 2020

Edition 1:1

ISBN 978-91-7929-880-7
ISSN 0345-7524
URL http://urn.kb.se/resolve?urn=urn:nbn:se:liu:diva-163501

Typeset using XeTeX

Printed by LiU-Tryck, Linköping 2020

POPULÄRVETENSKAPLIG SAMMANFATTNING

Den här avhandlingen presenterar en metod som kan mäta kroppens muskelvolym och även beräkna hur mycket fett som lagrats in i musklerna. Aktuell forskning visar att en minskning av muskelvolym samt en ökning av fettinlagringen i musklerna är kopplat till en rad olika sjukdomar och nedsättningar som till exempel kronisk smärta, diabetes, inflammation och åldrande. Även om dessa samband har visats genom forskning finns det idag inte tillräcklig kunskap om varför det sker och vilka som drabbas. Detta beror delvis på att bra metoder för att mäta muskler saknats. För att tidigt kunna ställa diagnos och sätta in rätt behandlingsmetod behövs teknik som noggrant kan se förändringar i muskelsammansättningen.

De metoder som idag används inom vården för att analysera muskler är främst baserade på att testa muskelfunktionen genom olika styrketester eller storleksmätning av exempelvis omkretsen kring överarmen. Problemet med dessa metoder är att muskelstyrka och omkrets båda är trubbiga mått. Muskelstyrkan är bara ett indirekt mått på hur mycket muskler du har. En förändring i omkrets säger heller ingenting om huruvida sammansättningen har ändrats. En minskning av muskelvolymen och en ökning av fettet skulle kunna ge oförändrat resultat på omkretsmätningen.

En magnetkameraundersökning är ett alternativ när vi behöver noggranna mätningar av kroppens muskler. Från magnetkameran kan vi skapa en tredimensionell bild av kroppens organ och fettdepåer. Eftersom fett och muskler ger olika signal kan vi också se fettinlagringen. Dock kvarstår utmaningar innan noggranna analyser av förändringar i muskelsammansättning är möjliga kliniskt och inom forskningen. Avhandlingen handlar om att lösa några av dessa utmaningar.

En utmaning är att göra resultatet från magnetkameraundersökningen kvantitativ. Du kommer inte att få samma intensitet på fettsignalen även om du samlar in data direkt efter varandra med exakt samma inställningar. Därför använder jag i denna avhandling en teknik som kan kalibrera varje bildelement efter hur mycket fett det avbildar, vilket gör den kvantitativ. Avhandlingen visar att analysmetoden ger samma resultat även om kameror med olika starkt magnetfält används eller om upplösningen ändras.

En annan utmaning är att göra analyskedjan effektiv. Att samla in och analysera data med en magnetkamera är tidskrävande. Att manuellt definera en muskel tar ca 45 minuter och är inte applicerbart i annat än ganska små studier. Därför utvecklades en metod för att automatisera definieringen av olika muskelgrupper. Den automatiska metoden används just nu för att anlaysera fyra olika muskler i världens hittills största bildstudie där magnetkamerabilder på 100 000 individer samlas in. Om analyserna istället gjorts helt manuellt skulle det ta runt 300 000 timmar, vilket motsvarar 175 år heltidsarbete.

Metoden applicerades även i en klinisk forskningsstudie. Individer med högre självupplevd kronisk smärta efter ett whiplash-våld mot nacken hade högre fettinlagring i sina nackmuskler jämfört med både individer som hade mindre ont och friska kontroller.

Avhandlingen visar att analysmetoden som presenteras är noggrann, effektiv och har klinisk relevans. Den har därmed potential att kunna användas i stora kliniska longitudinella studier med syfte att öka kunskapen om muskelrelaterade sjukdomar och nedsättningar som människor lider av idag.

ABSTRACT

Changes in muscle tissue composition, *e.g.* decrease in volume and/or increase of fat infiltration, are related to adverse health conditions such as sarcopenia, inflammation, muscular dystrophy, and chronic pain. However, the onset and progression of disease and the effect of potential intervention effects are not fully understood, partly due to insufficient measurement tools. For advanced knowledge regarding these diseases, an accurate and precise measurement tool for detecting changes in muscle composition is needed. The tool must be able to detect both local changes on specific muscles for investigating local injuries and generalized muscle composition changes on a whole-body level. Magnetic resonance imaging is an excellent tool due to its superior soft tissue contrast but is normally not quantitative, making it challenging to produce reproducible results. Furthermore, manual analysis of the vast amount of images produced is extremely time consuming and therefore expensive. The aim of this thesis was to develop and validate a new magnetic resonance imaging method for muscle volume quantification and fat infiltration estimation that would have the potential to be used in both large-scale studies and for analyzing small individual muscles.

The method development was divided into four main steps: 1) Rapid acquisition and reconstruction of data with sufficient resolution and calibration giving quantitative images where the relative fat content of each voxel (related to pure fat voxels) is attainable; 2) Automated muscle tissue classification based on non-rigid multi-atlas segmentation followed by probability voting to acquire the region of interest for each muscle; 3) Quantification of muscle tissue volume and fat infiltration from the classification step and the local fat signal; 4) Evaluation of the potential of the method in clinical studies.

In Paper I, a method for automatic muscle volume quantification of both whole-body and regional muscles, *i.e.* involving steps 1–3, is presented. The automated method showed good agreement compared to manual segmentation. It was robust to an 8-fold resolution difference using two different scanner field strengths. Papers II and III evaluated the clinical relevance and the need for developing methods with high-resolution images to answer the research questions regarding the effect of a whiplash trauma on the multifidus muscles. This involved steps 1–4. The method enabled acquisition of high-resolution data to distinguish the small multifidus muscles (Paper II). The paper also showed a higher fat infiltration in the multifidus muscles in individuals with severe self-reported disability compared to individuals with milder symptoms and to healthy controls. Furthermore, the local fat infiltration was also related to widespread muscle fat infiltration (Paper III). However, the difference in widespread muscle fat infiltration could not alone distinguish between the three different groups. Paper IV showed the robustness of fat infiltration estimation when changing flip angle, and thereby the T1 weighting, of the acquired images (steps 1–3). The higher flip angle also provided better noise characteristics. Therefore, this quantitative method can be used with higher flip angle, and thus a potentially better anatomical contrast, without losing accuracy or precision.

To conclude, this thesis presents a method that quantifies muscle volume and estimates fat infiltration robustly and reproducibly. The versatility of the method allows for both high-resolution images of small muscles and rapid acquisition of whole-body data. The method can be a useful tool in clinical studies regarding small individual muscles. Furthermore, the combination of being quantitative and automatic means that the method has potential to be used in longitudinal, multi-center, and large-scale studies for advanced understanding of muscular diseases.

Nog finns det mål och mening i vår färd -
men det är vägen, som är mödan värd.
— Karin Boye, *I rörelse*

Acknowledgments

Since I have been fortunate enough to have had not only excellent scientific input around me, but also practical and emotional support, there are quite a few I would like to acknowledge:

First of all I would like to thank my main supervisor *Magnus* for always having time to help me improve and for the patience when I needed it the most. I would also want to thank my co-supervisors: *Janne* for always seeking the most correct solution; and *Anneli* for insight from the medical point of view and for involving me as a project partner from start to end.

I thank all my co-authors for the fruitful discussions and hard work producing these papers. Special thanks to *Olof* for your visionary thoughts and to *Thobias* for answering all of my endless questions.

I have during this project been around inspiring, brave and knowledgeable people at IMT, CMIV, AMRA, and MSF. To name you all is motivated, yet not possible. I nevertheless highly appreciate all the discussions during fika, both the research related and the other. A special thanks to *Peter*, *Anders*, and *Agnetha* for believing in me when I did not.

Thank you *Gudrun*, *Sven-Gunnar*, *Ylva*, and *Tommy* for offering your babysitting services all over the world. And thank you *Chatarina* and *Svante* for offering the same at home.

Caroline, *Josefin*, *Ylva*, *Johan*, and *Jonas* for adventures and laughter that always recharge my batteries to their full potential. *Jenny* and *Maria*, for all conversations that widens my perspective and the will to keep on striving. *My Cem*, for tearing down the wall I didn't know I had built.

Mom and *Dad* for giving me a safe childhood, which in turn gave me the courage to be curious about the world. And, with help from *Anders*, for sharpening my argumentation skills during all dinner discussions throughout the years.

Laurent and *Hedvig*. You have been my best source for finding focus. You see, since I am not able to always be around you, I at least want the time away from you to be as meaningful as possible. I love you!

List of Papers

This thesis is based on the following papers, which will be referred to by their Roman numerals:

I. **Automatic and Quantitative Assessment of Regional Muscle Volume by Multi-Atlas Segmentation Using Whole-Body Water-Fat MRI**
Anette Karlsson, Johannes Rosander, Thobias Romu, Joakim Tallberg, Anders Grönqvist, Magnus Borga, and Olof Dahlqvist Leinhard
Journal of Magnetic Resonance Imaging (2015)

II. **An Investigation of Fat Infiltration of the Multifidus Muscle in Patients with Severe Neck Symptoms Associated with Chronic Whiplash-Associated Disorders**
Anette Karlsson, Olof Dahlqvist Leinhard, Ulrika Åslund, Janne West, Thobias Romu, Örjan Smedby, Peter Zsigmond, and Anneli Peolsson
Journal of Orthopaedic and Sports Physical Therapy (2016)

III. **The Relation Between Local and Distal Muscle Fat Infiltration in Chronic Whiplash Using Magnetic Resonance Imaging**
Anette Karlsson, Anneli Peolsson, James Elliott, Thobias Romu, Helena Ljunggren, Magnus Borga, and Olof Dahlqvist Leinhard
PLoS ONE (2019)

IV. **The Effect of Increased Flip Angle when Estimating Muscle Fat Infiltration Using Fat-Referenced Chemical Shift Encoded Imaging**
Anette Karlsson, Anneli Peolsson, Thobias Romu, Olof Dahlqvist Leinhard, Anna-Clara Spetz Holm, Sofia Thorell, Janne West, and Magnus Borga
Submitted for journal publication (2020)

Contributions

I. In this paper we present a quantitative and automatic method for measuring muscle volume on muscle groups and whole-body using multi-atlas segmentation. I did a major part of the method development, parts of the data acquisition and most of the data evaluation. I was the corresponding author and wrote most of the paper.

II. In this paper we investigated the muscle fat fraction and cross-sectional area in the small deep neck multifidus muscles, in a whiplash cohort. I was involved in the study design and did a significant part of the data acquisition. I did parts of the data reconstruction, and was the main responsible person for analyzing the data. I was the corresponding author and wrote most of the paper.

III. In this paper we investigated the relation between the small deep neck multifidus muscles and whole-body muscle composition in a whiplash cohort. I was the main responsible person in study design, data acquisition and analyzing the results. I was the corresponding author and wrote most of the paper.

IV. In this paper, we investigated how two different flip angles affect precision and accuracy using a fat-referenced chemical-shift encoded magnetic resonance imaging technique for muscle fat estimation. I was involved in designing the study. I did quality assurance of parts of the muscles and did all the data analysis. I am the corresponding author and wrote most of the paper.

Related Papers

The following papers are related publications not included in this thesis:

Peer Reviewed Full Length Articles

i. **Decreased muscle concentrations of ATP and PCR in the quadriceps muscle of fibromyalgia patients - A ^{31}P-MRS study**
Björn Gerdle, Mikael F. Forsgren, Ann Bengtsson, Olof Dahlqvist Leinhard, Birgitta Sören, **Anette Karlsson**, Vaslav Brandejsky, Eva Lund, and Peter Lundberg
European Journal of Pain (2013)

ii. **Test-retest reliability of automated whole body and compartmental muscle volume measurements on a wide bore 3T MR system**
Marianna S. Thomas, David Newman, Olof Dahlqvist Leinhard, Bahman Kasmai, Richard Greenwood, Paul N. Malcolm, **Anette Karlsson**, Johannes Rosander, Magnus Borga, and Andoni P. Toms
European Radiology (2014)

iii. **Consistent intensity inhomogeneity correction in water-fat MRI**
Thord Andersson, Thobias Romu, **Anette Karlsson**, Bengt Norén, Mikael F. Forsgren, Örjan Smedby, Stergios Kechagias, Sven Almer, Peter Lundberg, Magnus Borga, and Olof Dahlvist Leinhard
Journal of Magnetic Resonance Imaging (2015)

iv. **Intramuscular fat infiltration evaluated by magnetic resonance imaging predicts the extensibility of the supraspinatus muscle**
Hugo Giambini, Taku Hatta, Krzysztof R. Gorny, Per Widholm, **Anette Karlsson**, Olof Dahlqvist Leinhard, Mark C. Adkins, Chungeng Zhao, and Kai-Nan An
Muscle & Nerve (2018)

v. **Precision of MRI-based body composition measurements of postmenopausal women**
Janne West, Thobias Romu, Sofia Thorell, Hanna Lindblom, Emilia Berin, Anna-Clara Spetz Holm, Lotta Lindh Åstrand, **Anette Karlsson**, Magnus Borga, Mats Hammar, and Olof Dahlqvist Leinhard
PLoS ONE (2018)

vi. **The qualitative grading of muscle fat infiltration in whiplash using fat and water magnetic resonance imaging**
Rebecca Abbott, Anneli Peolsson, Janne West, James Elliott, Ulrika Åslund, **Anette Karlsson**, and Olof Dahlqvist Leinhard
The Spine Journal (2018)

vii. **Pathophysiology behind prolonged whiplash associated disorders: study protocol for an experimental study**
Anneli Peolsson, **Anette Karlsson**, Bijar Ghafouri, Tino Ebbers, Maria Engström, Margaretha Jönsson, Karin Wåhlén, Thobias Romu, Magnus Borga, Eythor Kristjansson, Hilla Sarig Bahat, Dmitry German, Peter Zsigmond, and Gunnel Peterson
BMC musculoskeletal disorders (2019)

Peer Reviewed Conference Abstracts

i. **Automated whole-body muscle segmentation & classification**
Anette Karlsson, Olof Dahlqvist Leinhard, Thobias Romu, and Magnus Borga
ISMRM workshop on Fat-Water Separation: Insights, Applications & Progress in MRI, Long Beach, CA, USA (2012)

ii. **High resolution isotropic whole-body symmetrically sampled two-point Dixon acquisition imaging at 3T**
Olof Dahlqvist Leinhard, Thobias Romu, **Anette Karlsson**, and Magnus Borga
ISMRM workshop on Fat-Water Separation: Insights, Applications & Progress in MRI, Long Beach, CA, USA (2012)

iii. **Automated whole-body muscle quantification based on a 10 min MR-exam**
Anette Karlsson, Olof Dahlvist Leinhard, Anna Vallin, Thobias Romu, and Magnus Borga
ISMRM 20th Annual Meeting & Exhibition, Melbourne, Australia (2012)

iv. **Whole-body muscle segmentation using multiple prototype voting**
Anette Karlsson, Johannes Rosander, Joakim Tallberg, Magnus Borga, and Olof Dahlqvist Leinhard
ISMRM 21st Annual Meeting & Exhibition, Salt Lake City, USA (2013)

v. **Automatic and quantitative assessment of total and regional muscle tissue volume using multi-atlas segmentation (1.5 T)**
Anette Karlsson, Johannes Rosander, Thobias Romu, Joakim Tallberg, Anders Grönqvist, Magnus Borga, and Olof Dahlvist Leinhard
ISMRM 22nd Annual Meeting & Exhibition, Milano, Italy (2014)

vi. **Water-fat separated MRI for detecting increased fat infiltration in the multifidus muscle in patients with severe problems due to chronic whiplash-associated disorder**
Anette Karlsson, Anneli Peolsson, Janne West, Ulrika Åslund, Thobias Romu, Örjan Smedby, Peter Zsigmond, and Olof Dahlqvist Leinhard

ISMRM 23rd Annual Meeting & Exhibition, Toronto, Ontario, Canada (2015)

vii. **Automatic and quantitative assessment of total and regional muscle tissue volume using multi-atlas segmentation**
Anette Karlsson, Johannes Rosander, Thobias Romu, Joakim Tallberg, Anders Grönqvist, Magnus Borga, and Olof Dahlqvist Leinhard
ISMRM 23rd Annual Meeting & Exhibition, Toronto, Ontario, Canada (2015)

viii. **Defining Sarcopenia with MRI-establishing threshold values within a large-scale population study**
Anette Karlsson, Jennifer Linge, Janne West, Jimmy Bell, Magnus Borga, and Olof Dahlqvist Leinhard *Radiological Society of North America (RSNA), 102nd Scientific Assembly and Annual Meeting, Chicago, Illinois, USA (2016)*

ix. **A potential pathophysiological link between generalized and localized muscle fat infiltration in chronic whiplash patients**
Anette Karlsson, Anneli Peolsson, James Elliott, Thobias Romu, Helena Ljunggren, and Olof Dahlqvist Leinhard *ISMRM 25th Annual Meeting & Exhibition, Honolulu, Hawaii, USA (2017)*

List of Abbreviations and Nomenclature

α	Flip angle
AT	Adipose tissue
B_0	Static magnetic field
B_1	Rotating magnetic field, also called RF-pulse
BMI	Body mass index
CIIC	Consistent intensity inhomogeneity correction
CSA	Cross-sectional area
CSE	Chemical shift encoded
DSC	Dice similarity coefficient
DXA	Dual-energy x-ray absorptiometry
FF	Fat fraction
FOV	Field of view
FWHM	Full width at half maximum
GRE	Gradient-recalled echo
ICC	Intraclass correlation
ip	In-phase
L	Liters
M_{AUT}	Automatically acquired muscle mask
M_{M}	Muscle mask
M_{MAN}	Manually acquired muscle mask
M_{FF}	Fat-free muscle mask
M_{L}	Lean muscle mask
MFI	Muscle fat infiltration

$\mathrm{MFI}_{f_{\mathrm{RFC}}}$	Fat-referenced muscle fat infiltration
$\mathrm{MFI}_{\mathrm{PDFF}}$	Fat-referenced muscle fat infiltration converted to PDFF.
MR	Magnetic resonance
MRI	Magnetic resonance imaging
NDI	Neck disability index
op	Opposed phase
PD	Proton density
PDFF	Proton density fat fraction
ppm	parts per million
PSR	Phase-sensitive reconstruction
RF	Radio-frequency
RFC	Relative fat content
ROI	Region of interest
sd	standard deviation
SNR	Signal-to-noise ratio
s_w	within-subject standard deviation
T	Tesla
T_1	Longitudinal relaxation time
T_2	Transversal relaxation time (caused by spin-spin relaxation)
T_2^*	T_2 in combination with transversal relaxation due to B_0 inhomogeneities
TE	Echo time
TR	Repetition time
$V_{M_{\mathrm{M}}}$	Muscle mask volume
$V_{M_{\mathrm{FF}}}$	Fat-free muscle mask volume
$V_{M_{\mathrm{L}}}$	Lean muscle mask volume
WAD	Whiplash-associated disorders

Contents

List of Figures

List of Tables

"Begin at the beginning," the King said gravely, "and go on till you come to the end: then stop."

— Lewis Carroll, *Alice in Wonderland*

1

Introduction

This chapter starts by motivating the need of this thesis. It follows with the main goal and ends by outlining the rest of the thesis.

1.1 Motivation

The ability to accurately and precisely measure changes in muscle tissue volume is important for advanced knowledge regarding diseases, syndromes, and disorders such as sport injuries [1], muscle dystrophies [2–5], inflammatory myopathies [6] or sarcopenia [7–9]. Furthermore, inflammation [10], and aging [11] in addition to other health conditions such as type II diabetes [12], fibromyalgia [13] and chronic pain [14] have been shown to relate to an increase of fatty tissue infiltrated inside the muscle fascia. However, the impact, causes, and progress of changes in muscle composition are not yet fully understood.

One example where detailed knowledge regarding muscle volume and fat infiltration is of importance is in patients suffering from chronic whiplash-associated disorders (WAD). Half of the individuals having WAD after being involved in a motor vehicle accident will never fully recover [15]. Although research has found a higher fatty infiltration in the deep neck muscles, especially the multifidus muscles, in patients with chronic disorders after the whiplash trauma [16, 17], it is not clear on the causes.

In order to answer the specific questions of WAD and questions for other muscle related disorders, a method that can accurately track changes in muscle composition is needed. There are many methods to more or less indirectly measure changes in muscle tissue. One way to diagnose different muscle diseases is by using muscle biopsy [18] but the method is invasive and sensitive to anatomical variances in the muscles. Strength tests, physical ability tests, and limb circumference are beneficial due to their availability and low costs [8]. However, these methods are neither accurate nor precise due to high

variability [4, 5, 8] and limb circumference is also limited to muscles in the extremities and can not be used for *e.g.* the deep muscles in the neck. Furthermore, studies on young boys with Duchenne muscular dystrophy have shown that an increase in fat infiltration can be detected up to two years before a decrease in physical abilities can be detected [4, 5]. Ultrasonic imaging and surface electromyography (where the electrodes are attached to the skin) are both non-invasive and available techniques and can measure real-time muscle function. However, non-invasive electromyography is limited to superficial muscles and neither are feasible for extracting fat infiltrated in the muscles. Another rapid and relatively available technique is dual-energy x-ray absorptiometry (DXA). However, the technique only provides 2D projections of the imaged object. This means that no accurate separation between different muscle groups can be obtained. For the same reason it is not possible to distinguish fat infiltrated in the muscles from other fat compartments such as subcutaneous fat using DXA. Tomographic methods such as computed tomography and magnetic resonance imaging (MRI) provide the possibility for detailed 3D analysis of the human body. MRI also offers superior soft tissue contrast and does not use ionizing radiation, which makes it a great choice for advanced muscle composition imaging. Drawbacks with MRI are availability and cost [8]. Also, without post-processing, the MR images do not contain quantitative information.

Today, the number of MR scanners increase worldwide, including an increasing number of 3 T scanners, which enables high-resolution images. High-resolution images are required for segmentation of small muscles such as the deep multifidus muscles in the neck. However, availability alone will not solve the problem. For muscle composition analysis to be feasible in more than smaller research studies, a time-efficient analysis is needed. This is important both in acquiring data and finding the muscles in the acquired images, since scanner time and expert radiologist time are both expensive and not easily available. At the starting point of this thesis, only a few studies presenting methods for automated muscle analysis were found [19–22]. Most methods used morphological operations on parts of the body [19, 20] or on the whole-body [21]. The drawback of morphological methods is that such methods are based on *classification* of different tissues, meaning that it is hard to separate different muscles groups. Baudin *et al.* proposed a technique based on random walks and prior knowledge as an approach to segmenting different muscles apart from each other, but only in the lower extremities [22]. Therefore, a method for automated regional and whole-body muscle *segmentation* would significantly improve the potential for muscle composition analysis.

Another challenge is to separate lean muscle tissue from fat infiltrated in the muscle. Since both the muscle volume and fatty infiltration are related to several syndromes as mentioned earlier, the muscle analysis needs to be able to characterize different tissue compartments within the muscle. The method needs to be both accurate and precise. One of the main challenges is

to obtain quantitative information of muscle volume and fat infiltration. With quantitative information, higher accuracy and precision may be obtained than when a radiologist qualitatively draws conclusions on the amount of *e.g.* fat in muscles. Furthermore, due to the time-consuming task of segmenting muscles manually, analyses of muscles have been performed on a limited number of cross-sectional slices. This approach increases the sensitivity to accurate slice position. With whole-volume 3D images, that uncertainty can be minimized.

As mentioned before, MRI varies in intensity, and different parameter settings will affect contrast, signal-to-noise ratio (SNR), and image weighting. Therefore, a method insensitive to changes in field strength and scanner resolution will make the versatility of the method much greater for multi-center studies. Furthermore, even *if* some MR-parameters are set identical, the actual parameter is not certain to be the same. One example is flip angle. Inhomogeneities in the magnetic field might influence the *true* flip angle and hence also the contrast of the images. Therefore, also insensitivity to flip angle is important for a quantitative measurement. Lastly, the ability to acquire whole-volume images should minimize effects of noise, slice selection, and anatomical variance.

In order to limit the complexity of a quantitative body composition analysis method using MRI, it can be broken down to four main steps [23]:

1. Data acquisition and reconstruction – acquiring MR images that enable fat quantification,

2. Tissue segmentation – finding the target tissue of interest in an effective way,

3. Feature extraction – extracting quantitative information regarding biomarkers,

4. Data analysis – clinical studies or applications (*e.g.* cross-sectional or longitudinal studies) for analyzing different cohorts' muscle composition.

The different steps are easily translated for *quantitative muscle composition analysis*. Since each individual step needs to be accurate and precise, it is better to view the different steps as a linked chain, where each link will influence all other. For example, the scanner parameters affect which conclusions are drawn in the data analysis step. Therefore, knowledge regarding potential errors in the entire chain is crucial. Optimizing one link with respect to the above mentioned challenges needs to be done in consideration to all the other links.

This thesis therefore presents an analysis method including all four links; from data acquisition to data analysis where the requirements of being *accurate*, *precise*, and *effective* are evaluated.

1.2 Aims

The main aim of this thesis was to develop and validate methods for rapid whole-volume acquisition for muscle composition analysis including small individual muscles as well as larger muscle regions and total muscle tissue volume to meet the specific requirements of potential applications. The specific aims of this thesis were:

- to develop a rapid whole-body MRI acquisition method for quantitative assessment of total and regional muscle composition analysis, *i.e.* muscle volumes and fat infiltration;
- to evaluate the accuracy and precision of the developed method by alternating field strength, resolution, and flip angle;
- to develop and evaluate a high-resolution whole-volume acquisition method for analysis of the multifidus muscles in the deep neck muscles for investigation of the potential for clinical applications of muscle composition analysis to patients with severe neck pain associated with chronic WAD.

1.3 Delimitations

The development and optimization of an automatic muscle composition analysis were delimited to larger muscle groups with whole-volume coverage. Therefore, automatic segmentation of the small multifidus muscles was not included within the work of this thesis.

1.4 Thesis Outline

This thesis consists of seven chapters. The first chapter motivates the need and specifies the main objectives for the thesis. Chapters 2–5 cover the four different links for quantitative muscle composition analysis: Chapter 2 concerns data acquisition including post-processing into fat-referenced images; in Chapter 3, the automatic muscle tissue segmentation is presented; Chapter 4 explains the feature extraction from segmented images into quantitative lean tissue volume and fat infiltration; and Chapter 5 presents the technical evaluation of accuracy and reproducibility with respect to different field strengths, image resolutions, and flip angles. Chapter 6 presents results from two clinical studies investigating different aspects of muscle fat infiltration in patients with chronic WAD. In Chapter 7, the results of the whole muscle composition chain (steps 1–4 described in Chapters 2–5) are discussed and potential future developments and applications of the method are presented.

2

Fat-Referenced Chemical Shift Imaging

The first step of the muscle composition analysis is data acquisition including post-processing of the signal into quantitative information. This chapter gives an overview of the acquisition from the scanner, separation of water from fat and lastly, the calibration of the fat signal into quantitative information. The chapter does not cover all theory of MRI, but rather highlight aspects important for understanding quantitative chemical shift imaging and post-processing that may affect the muscle composition analysis. A full description of the algorithms used for water-fat separation and fat-referenced calibration used in this thesis can be found in Thobias Romu's eminent PhD thesis [24] but is also summarized in Section 2.3 and Section 2.4.

2.1 Magnetic Resonance Imaging

Both water and fat contain hydrogen protons (H^+). Hydrogen protons have a physical property called spin and can be seen as small individual magnets with their own magnetization vectors. In the absence of an external magnetic field, the direction of each of these magnetization vectors is random, *i.e.* the net magnetization vector, M_0, is zero. In MRI, the protons are placed into a strong static magnetic field, B_0, which is applied along an axis denoted the z-axis. The applied field will interfere with the 'small magnets' (protons). After reaching equilibrium, the z-component of the protons' magnetization vectors have a slightly increased likelihood to be positive. Also, the proton precesses around the z-axis at a specific angular frequency, called the Larmour frequency given by

$$\omega = -\gamma B_0, \tag{2.1}$$

where γ is the gyro-magnetic ratio in $(rad/(s \cdot T))$ and the unit for B_0 is Tesla (T). The gyro-magnetic ratio is a constant for each proton with a spin. However, the precession frequency around the B_0-axis is still varying for hydrogen protons, since the protons are shielded by the molecule's electron

shells and will therefore precess slightly different depending on what molecule structure it is bound to. This slight difference in precession frequency is defined by

$$\delta_j = -\frac{\omega_{\text{ref}} - \omega_j}{\omega_{\text{ref}}}, \tag{2.2}$$

where ω_{ref} is the precession of a reference tissue, ω_j is the precession of the tisuse j and δ_j is the *chemical shift* between ω_{ref} and ω_j. The chemical shift is small in comparison to the Larmour frequency of the hydrogen proton and therefore often referred to in parts per million (ppm). The two hydrogen protons in every water molecule experience the same electronic shielding, while the hydrogen protons bound to the more complex lipid (fat) molecules experience different electronic shieldings. This results in several different resonance frequencies for the lipid molecule and 6-7 different resonance frequencies have been observed [25, 26]. This chemical shift between the fat and water molecules is the feature utilized for muscle composition analysis when using water-fat separation techniques.

Under the influence of B_0, the protons precess incoherently. To create a coherent precession, a rotating magnetic field, B_1, is applied in the plane perpendicular to B_0, denoted the xy-plane. B_1 rotates at (or very close to) the Larmour frequency. This creates coherence of the precession. Hence, M_0 will be *tipped* from the z-axis into the xy-plane where it rotates at the Larmour frequency. The offset angle between the tipped magnetization vector and the z-axis is called the flip angle, α. The flip angle is a parameter that needs to be considered in muscle composition analysis and will be addressed later and is also the main focus in Paper IV.

The rotating net magnetization in the xy-plane induces currents in receiver coils, and that signal is the basis for MRI. The signal is often acquired in quadrature, meaning that different receiving coils are used and designed to detect the induced current from two directions, which are orthogonal from each other. Hence, the MR signal is complex and has both magnitude and phase information, which is a feature used in chemical shift imaging for water-fat separation.

Another common name for the rotating B_1 is an RF-pulse; 'RF', since the Larmour frequency in field strengths of clinical scanners (1.5 T and 3 T) is within the radio frequency range; and 'pulse' since it is only applied under a short period of time. When the applied field is turned off, two types of *relaxations* occurs: longitudinal (z-direction) and transversal (xy-plane). The longitudinal relaxation (also called spin-lattice relaxation or T_1-relaxation) occurs due to loss of energy caused by thermal motion. The transversal relaxation (also called spin-spin relaxation or T_2-relaxation) occurs since the protons de-phase in the xy-plane due to exchange of energy. After full relaxation, the net magnetization, M_0, is again aligned with B_0 and a new RF-pulse may be applied.

The time it takes to reach equilibrium after turning off the RF pulse depends on the T_1-relaxation (since $T_2 \ll T_1$ for most tissues). T_1 is the time it takes for the z-component of the net magnetization, M_z (in a certain tissue) to reach 63% of its maximum value at equilibrium (M_0) (after turning off the RF-pulse). T_2 is the time while (in a certain tissue) the xy-component still maintains 37% of M_0, after turning off the RF-pulse.

T_1 and T_2 are tissue dependent. For example, T_1 is shorter for fat than for muscles. T_1 has been estimated to $T_{1,f} \approx 371$ ms in fat and $T_{1,m} \approx 1,420$ms in muscles [27]. Furthermore, some imaging methods are sensitive to B_0 inhomogeneities (spatial variations in B_0), resulting in faster de-phasing in the transversal plane. This is called T_2^* which is always less than T_2 for a certain tissue. A third property of tissue is the proton density (PD) of a tissue *i.e.* the total amount of (MR-visible) protons in the tissue. All these three properties affect the signal magnitude detected in the receiver coils.

To be able to achieve spatial information about the location of the detected signal, the MR scanners use gradient coils. The gradient coils induce a location-specific change of Larmour frequency, which can be detected by the receiver coils. While this thesis does not go into details of sampling and reconstructing the MR image, the gradient coils are of interest for water-fat separated MRI. The gradient coils can be used to de-phase and re-phase the signal so that signal echoes occur at specific echo times, TE, without the use of an additional RF-pulse. The combination of RF-pulses and gradients is called MR sequence. The MR sequence is repeated and the time between rotating RF-pulses in the xy-plane is called repetition time, TR.

Signals are sampled by the receiver coils at each TE. Since different tissues have different T_1-relaxation, T_2-relaxation and PD, the choice of TE, TR and α affect the contrast between different tissues. By changing TE, TR, and α, different *weightings* of the signals can be achieved. If the contrast between the images is dominated by the difference in T_1-relaxation, the images becomes T_1-*weighted*. Similarly, if the contrast is dominated by difference in T_2-relaxation they are T_2-*weighted* and the images become *PD-weighted* if the contrast is dominated by differences in PD.

MR sequences using the gradient coils to de-phase and re-phase the signal in order to create echoes are called Gradient Recalled Echo (GRE) sequences. One of the main benefits of GRE sequences is that multiple echoes can be acquired for each repetition, enabling time efficient acquisitions. Furthermore, by using *spoiled* GRE sequences the transverse magnetization (M_{xy}) is canceled out prior to each RF pulse [28]. This allows for very short TR without residual coherent transverse magnetization occurring from previous RF-pulses, resulting in a T_1-weighted contrast [28].

The complex GRE signal model rotating at the reference resonance frequency (ω_{ref}) in a voxel at position r for a specific choice of the parameters TR, and α is described by

$$s_{\text{GRE}} = k \sum_j g_j \cdot p_j \cdot e^{-i\gamma(B_0 \cdot \delta_j + \Delta B_0)\text{TE} - \text{TE}/T^*_{2,j}} \tag{2.3}$$

where

k	models factors such as eddy currents and coil sensitivity and depends on r and TE.
g_j	models the saturation of the signal at a specific proton j. It depends on TR, TE and α, where the exact value of α is dependent on r due to inhomogeneties in B_1.
p_j	is the number of protons belonging to tissue type j.
$e^{-i\gamma(B_0 \cdot \delta_j) \cdot \text{TE}}$	describes the contribution of the relative phase shift of tissue j to the reference tissue.
$e^{-i\gamma(\Delta B_0) \cdot \text{TE}}$	describes the phase error due to inhomogeneties in B_0.
$e^{-\text{TE}/T^*_{2,j}}$	describes the signal loss due to T_2^* at a specific TE for tissue j.

All of the parameters in Equation 2.3 need to be accounted for in water-fat separated imaging. This can be done by simplifying the model, assuming constant values and by correction of e.g. phase errors.

2.2 Water-Fat Separated Imaging

In water-fat imaging using GRE it is often assumed that all of the signal comes from either fat or water. The resonance frequency of water is often used as reference and the different resonance frequencies of the lipid molecule are expressed as ppm from water. See Figure 2.1 for an illustration of how a frequency spectrum in a voxel containing water and fat molecules could look like.

Equation 2.3 can be expressed using ω_{water} as the reference resonance frequency and assuming a constant lipid model where a_l is the relative amplitude at lipid l, see Figure 2.1. The signal equation can be further simplified by assuming a single T_2^*-term since most of the human tissue is either water-dominant or fat-dominant [29]. With the above modifications the signal equation can be expressed as

$$s = \left(w + f \cdot \sum_l a_l \cdot e^{-i\gamma B_0 \delta_l \cdot \text{TE}}\right) e^{-i\gamma \Delta B_0 \cdot \text{TE} - \text{TE}/T_2^*} \tag{2.4}$$

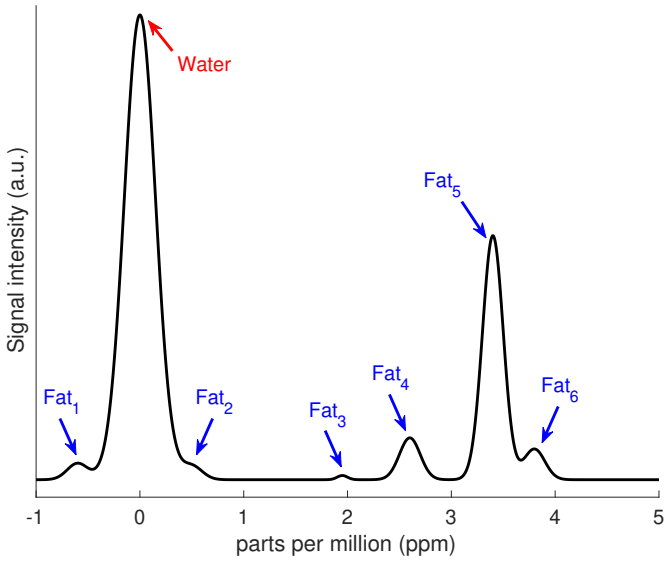

Figure 2.1: An illustration of how a hydrogen proton spectrum containing water and fat can look like using water as the reference resonance frequency ω_{ref}. Water protons share the same electron shielding and only a single peak will be found. For fat, six different resonance frequencies are often found (at $B_0 = 3$ T) due to the more complex molecule structure. The area under each peak in the spectrum corresponds to the amount of protons precessing at that resonance frequency.

where

$$w = k \cdot g_w \cdot p_w, \tag{2.5a}$$

$$f = k \cdot g_f \cdot p_f \tag{2.5b}$$

and g_w is the saturation level of the water signal, g_f is the saturation level of the fat signal, p_w is the total number of protons bound to water and p_f is the number of protons bound to fat.

Chemical shift encoded (CSE) MRI for water-fat separation was first reported by Thomas W. Dixon in 1984 [30]. The basic theory of CSE-MRI state that the signal contribution from water and fat can be separated into two different images using the information from the magnitude and phase images in the GRE-sequence based on carefully chosen TEs.

Dixon proposed 2 echoes (which is often denoted 2-point Dixon) acquired *symmetrically* [30]. Symmetrical acquisition means that one TE is chosen when the fat and water signal are in *opposite phase*, *op*, (the angle between the signal vectors are π) and one when the fat and water signal are *in-phase*, *ip*

(where the angle between the fat and water vectors is 0). Today, CSE-MRI has evolved from the original Dixon imaging to also include both asymmetrically echoes and multi-echo acquisitions with n number of TEs. One advantage of the multi-echo CSE-MRI is that T_2^* can be estimated for each data instead of assuming the same T_2^* between subjects for a certain tissue. However one drawback is longer TRs and hence, longer acquisition times.

Due to ΔB_0 and k, a phase error $(-i\gamma \cdot \Delta B_0 \cdot \mathrm{TE}_{op})$ occurs that needs to be determined before water-fat separation. If the phase error is known and assuming no T_2^* relaxation, the water and fat can be directly calculated from a symmetrically sampled 2-point Dixon sequence as:

$$2 \cdot w = \| ip \|_2 + op \cdot e^{i\gamma \cdot \Delta B_0 \cdot \mathrm{TE}_{op}} = (w + f) + (w - f) \tag{2.6a}$$

$$2 \cdot f = \| ip \|_2 - op \cdot e^{i\gamma \cdot \Delta B_0 \cdot \mathrm{TE}_{op}} = (w + f) - (w - f) \tag{2.6b}$$

It is essential for water-fat separation to solve the phase error accurately for a quantitative muscle composition analysis to work. Many techniques exist [31–36] and today the MR scanners' on-line software also provide robust water-fat separations. The choice of method might put constraints on the GRE sequence since some require multi-echo acquisitions and other call for asymmetrical acquisition. Those constraints can influence the choice of method if *e.g.* rapid acquisition is desirable as multi-echo requires longer acquisition times. In this thesis, a water-fat separation technique called phase-sensitive reconstruction (PSR) was used [37, 38].

2.3 Phase-Sensitive Reconstruction

When data for this thesis were acquired, no available method for water-fat separation for whole-body 2-point symmetrically acquired images at the MR scanners existed [24]. Therefore, the PSR method was used, previously explained by Rydell *et al.* [37] and Romu *et al.* [38]. Briefly, the method uses a few assumptions on the local phase information. Clusters of connected tissue can be acquired by assuming that the phase outside tissue will only be random due to the complex noise.

The next step is finding the phase error, see Figure 2.2*A* where the (wrapped) phase is seen to the left and the phase error corrected image is seen next to it, on the right. Both the magnitude image and the phase image are shown, where the phase has been color coded. The phase-unwrapping was done by solving a Poison equation, first explained by Song *et al.* [39]. The third step was to identify the classification (water or fat) of each cluster of connected tissue. This is illustrated in 2.2*B*, where classifications of the different stacks are still unknown. The PSR algorithm is based on the assumption that the images are T_1-weighted, *i.e.* the fat signal will have a higher magnitude

than the water signal [24]. The final result of the PSR algorithm is illustrated in 2.2*C*.

In this thesis, whole-body data were acquired using multiple 3D image stacks with a spatial overlap in the z-direction. The final step to obtain a water-fat separated image therefore included an image stack fusion when multiple stacks data are acquired, Figure 2.2$C \Rightarrow D$. Observe that the fused image volumes are shorter since the stack overlap is removed.

2.4 Quantitative Chemical Shift Imaging

After water-fat separation, the signals from water protons and fat protons can be analyzed separately. However, the signals are not quantitative. First, the signals have spatially varying intensities due to differences in B_0 and experimental factors, k, see Figure 2.2*D*. Second, the contrast between fat and water is more dependent on T_1-weighting rather than different number of protons in the voxels.

If assuming a perfectly spoiled GRE sequence, and taking the multiple fat resonance frequencies into account, the signal from water protons and fat protons in a voxel can be described by:

$$s_w = k \cdot p_w \cdot g_w \cdot e^{-\mathrm{TE}/T_2^*} = k \cdot p_w \frac{\sin(\alpha)(1 - e^{-\mathrm{TR}/T_{1,w}})}{(1 - \cos(\alpha)e^{-\mathrm{TR}/T_{1,w}})} \cdot e^{-\mathrm{TE}/T_{2,w}^*} \tag{2.7a}$$

$$s_f = k \cdot p_f \cdot g_f \cdot e^{\mathrm{TE}/T_2^*} = k \cdot p_f \frac{\sin(\alpha)(1 - e^{-\mathrm{TR}/T_{1,f}})}{(1 - \cos(\alpha)e^{-\mathrm{TR}/T_{1,f}})} \cdot e^{-\mathrm{TE}/T_{2,f}^*}. \tag{2.7b}$$

The parameters that can be controlled in Equations 2.7a and 2.7b are TR, TE and α. As can be seen, TE will influence the T_2^*-weighting of the image. T_2^* can however be corrected for in the signal equation, leading to a flexibility in TE. The T_2^* correction can be done by either estimating the signal decay using a multi-echo sequence or by assuming that T_2^* is constant between individuals at a specific field strength in a certain tissue (necessary in 2-point Dixon), see Equation 2.13.

TR influences the T_1-weighting of the images and long TRs can be used to minimize the effect. However, long TRs are not always feasible since they result in long acquisition times, *i.e.* including long breath-holds (breath-holds are needed when acquiring images in the abdominal region since MRI is very sensitive to motion). An alternative is to alter α, since the flip angle also influences the T_1-weighting of the images. When α is small, the term $\cos(\alpha)$ will be approximately equal to 1 and the signal will not be significantly affected by differences in T_1 between water and fat (see Equations 2.7a and 2.7b).

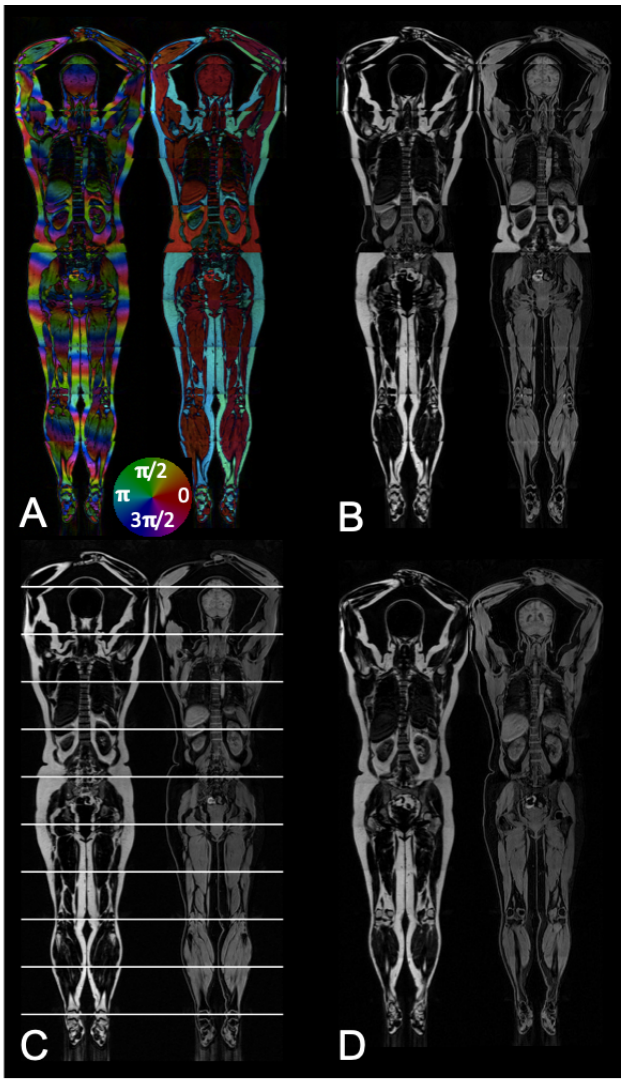

Figure 2.2: A schematic illustration of the different steps of the phase-sensitive reconstruction (A-C) followed by an illustration of the merging of multi-stack volumes into two water-fat separated whole-body volumes.

Proton Density Fat Fraction

When compensating for T_2^* in combination with a small flip angle (α = 2–3° at 3 T), the images will become PD-weighted, meaning that mainly the difference in proton density will affect the contrast (assuming that k will affect water and fat protons equally). By using these parameter settings, the fraction of

MR-visible fat protons in relation to the total amount of MR-visible protons can be calculated, a method called Proton density fat fraction (PDFF) [40]. The PDFF in a voxel is then calculated as

$$\text{PDFF} = \frac{p_f}{p_f + p_w} \approx \frac{s_f}{s_f + s_w}. \tag{2.8}$$

This method is self-calibrating, where inhomogeneities are accounted for since PDFF is calculated in each voxel. This results in a quantitative measure of the fraction of fat inside a voxel.

However, the small flip angle will decrease the SNR since less signal will be detected in the receiver coils due to less contribution of the signal in the xy-plane. If high SNR is required, two flip angles (one larger and one small) can be acquired so that correction for the overestimation of fat due to the T_1-bias can be performed [41]. However, this will also double the acquisition time.

Fat-Referenced Calibration

Another approach to obtain a quantitative measurement of the fat content in a certain tissue is to calibrate the image using pure adipose tissue voxels as a reference [42, 43]. The calibration technique used on the whole-body images in this thesis is called consistent inhomogeneity intensity correction (CIIC) and has been described by Dahlqvist Leinhard *et al.* [43], Romu *et al.* [44], and Andersson *et al.* [45]. Briefly, the images were calibrated using normalized averaging, which is a convolution technique that also accounts for the certainty in the information [24]. After calibration, pure adipose tissue voxels are set to the intensity value of 1, meaning that the fat content in a certain voxel is in relation to a voxel of pure adipose tissue.

The effect of the removal of inhomogeneities is illustrated in Figure 2.3 where the left image show data before correction and the right show data after correction using CIIC.

The calibrated image is called the fat-referenced, f_{RFC} image. The f_{RFC} for a certain voxel can be calculated by

$$f_{\text{RFC}} = \frac{f}{f_{\text{ref}}} \tag{2.9}$$

where f_{ref} is the reference fat signal defined by interpolating the fat signals from the reference adipose tissue. The method can also be applied to remove some inhomogeneity in the original water image.

f_{RFC}, can also be explained as the volume fraction of fat in relation to the volume of fat in the reference tissue [24]. Assuming a compartment consists of three different types of tissues: (MR-visible) fat, (MR-visible) water and MR-

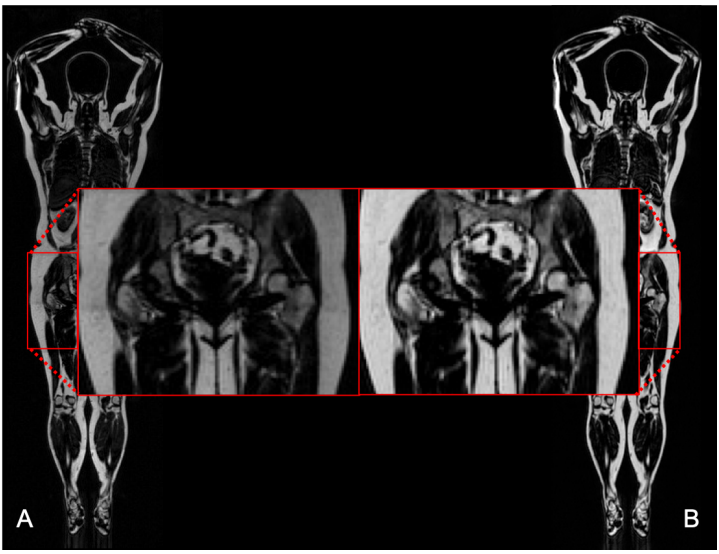

Figure 2.3: An illustration of the effect of image calibration using fat as its own reference. In A, the result after water-fat separation is shown. The image has a locally varying fat intensity due to B_0 inhomogeneities and experimental factors such as coil sensitivity. In B, the result after applying the consistent intensity inhomogeneity correction (CIIC) where the fat signal is calibrated using pure adipose tissue voxels as a reference is shown.

invisible tissue. Then the volume fraction in a certain voxel can be expressed as

$$V_f + V_w + V_0 = 1, \tag{2.10}$$

where V_f is the volume fraction of fat, V_w is the volume fraction of water and V_0 is the volume fraction of non-visible tissue. Equation 2.5 can for a certain voxel then be expressed as

$$w = k \cdot g_w \cdot p_w = k \cdot g_w \cdot V_w \cdot n_w \tag{2.11a}$$
$$f = k \cdot g_f \cdot p_f = k \cdot g_f \cdot V_f \cdot n_f \tag{2.11b}$$

where n_w is the number of water-bound protons in the voxel, and n_f is the number of lipid-bound protons in the same voxel. The ratio between n_w and n_f has been reported close to 1 ($n_w/n_f \approx 0.98$) [46]. If the spatial distance between f and f_{ref} is small, $k_f \cdot g_f$ and $k_{\text{ref}} \cdot g_{\text{ref}}$ can be assumed to be fairly equal, *i.e.* $k_f \cdot g_f \approx k_{\text{ref}} \cdot g_{\text{ref}}$. Then, Equation 2.9 can be expressed as

$$f_{\text{RFC}} = \frac{f}{f_{\text{ref}}} = \frac{k \cdot g_f \cdot V_f \cdot n_f}{k_{\text{ref}} \cdot g_{\text{ref}} \cdot V_{\text{ref}} \cdot n_{\text{ref}}} = \frac{V_f}{V_{\text{ref}}}. \tag{2.12}$$

Hence, f_{RFC} is the amount of fat in a certain tissue in relation to the equivalent amount of fat in the reference tissue, *i.e.* the amount of fat in pure adiopose tissue (AT).

The last part of 2-point Dixon fat-referenced imaging (used in Paper I-Paper III) is correction of T_2^*. As mentioned earlier, the T_2^*-decay cannot be estimated using only 2 echoes. However, assuming a constant T_2^* for a certain tissue, the bias can be compensated for. In this thesis, the correction of the T_2^*-decay is calculated by

$$f_{\text{RFC}} = f_{\text{2PD,RFC}} + w_{\text{2PD,RFC}} \frac{e^{-\text{TE}_{ip}/T_{2,w}^*} - e^{-\text{TE}_{op}/T_{2,w}^*}}{e^{-\text{TE}_{ip}/T_{2,w}^*} + e^{-\text{TE}_{op}/T_{2,w}^*}}, \tag{2.13}$$

where $f_{\text{2PD,RFC}}$ and $w_{\text{2PD,RFC}}$ is the calibrated fat and water signal respectively [24].

Fat-Referenced Imaging in Relation to PDFF

Fat-referenced imaging estimates the fat amount in relation to the amount of fat in adipose tissue. PDFF instead calculates the fraction of fat protons in relation to the total number of water and fat protons. However, the correlation between the techniques is high [47] and R_{RFC} can be related to PDFF using a few simplifications. By approximating that $n_w/n_f \approx 1$ [46] and that the volumes of non-visible protons in fat, $V_{0,f}$, and in the reference tissue, $V_{0,\text{ref}}$, are equal, then PDFF can be related to f_{RFC} by

$$\begin{aligned}
\text{PDFF} &= \frac{p_f}{p_f + p_w} \\
&= \frac{p_f}{p_f + p_w} \frac{p_{f,\text{ref}}}{p_{f,\text{ref}} + p_{w,\text{ref}}} \frac{p_{f,\text{ref}} + p_{w,\text{ref}}}{p_{f,\text{ref}}} \\
&= \frac{p_f}{p_{f,\text{ref}}} \frac{p_{f,\text{ref}} + p_{w,\text{ref}}}{p_f + p_w} \frac{p_{f,\text{ref}}}{p_{f,\text{ref}} + p_{w,\text{ref}}} \\
&= f_{\text{RFC}} \frac{p_{f,\text{ref}} + p_{w,\text{ref}}}{p_f + p_w} \text{PDFF}_{\text{ref}} \\
&= f_{\text{RFC}} \frac{n_{f,\text{ref}} \cdot V_{f,\text{ref}} + n_{w,\text{ref}} \cdot V_{w,\text{ref}}}{n_f \cdot V_f + n_w \cdot V_w} \text{PDFF}_{\text{ref}} \\
&= f_{\text{RFC}} \frac{V_{f,\text{ref}} + \frac{n_{w,\text{ref}}}{n_{f,\text{ref}}} \cdot V_{w,\text{ref}}}{V_f + \frac{n_w}{n_f} \cdot V_w} \text{PDFF}_{\text{ref}} \\
&\approx f_{\text{RFC}} \frac{1 - V_{0,\text{ref}}}{1 - V_0} \text{PDFF}_{\text{ref}} \\
&\approx f_{\text{RFC}} \cdot \text{PDFF}_{\text{ref}}
\end{aligned} \tag{2.14}$$

Using the PDFF of the reference tissue, *i.e.* adipose tissue, f_{RFC} can be converted to PDFF and used for muscle composition analysis without the con-

straint to use either low flip angles or long acquisition times (long TR or dual-flip angle acquisitions), which was also used in Paper IV.

2.5 Data Acquisition

In this thesis, four different protocols were used: One whole-body coverage protocol acquired at a 1.5 T scanner (Paper I); one whole-body coverage protocol at a 3 T scanner (Paper I and Paper III); One rapid whole-body protocol (used in Paper IV); and one high-resolution neck protocol (used in Paper II and Paper III). Acquisition details, including the constant values used for PDFF_{ref} and T_2^* (when applicable), of the four protocols are presented in Table 2.1.

	Whole-Body 1.5 T Paper I	Whole-Body 3 T Paper I, Paper III	Rapid Whole-Body Paper IV	Neck Paper II, Paper III
Scanner Parameters				
Scanner	Philips Achieva	Philips Ingenia	Philips Ingenia	Philips Ingenia
Field strength	1.5 T	3 T	3 T	3 T
Sequence	3D spoiled GRE	3D spoiled GRE	3D spoiled GRE	3D spoiled GRE
Echo times (ms)	2.3/4.6	1.15/2.3	1.15/2.30/3.45/4.60	3.66/7.24
Repetition time (ms)	6.57	3.78	6.99	10
Flip angle (°)	13	10	5/10	10
Number of stacks	11	10	10	1
Image stack overlap (mm)	28	30	25	n/a
Expiration breathhold (s)	17	26	17	n/a
Acquired resolution (mm^3)	$3.5 \times 3.5 \times 3.5$	$1.75 \times 1.75 \times 1.75$	$2.5 \times 2.5 \times 4$	$0.75 \times 0.75 \times 0.75$
Field of view (cm^3)	$53 \times 53 \times 206$*	$56 \times 56 \times 185$*	$58 \times 56 \times 176$*	$53 \times 53 \times 19.5$
Acquisition time (min)	10	25	8	9
Constants				
T_2^* (ms)	23.9	23.9	estimated	23.9
$PDFF_{ref}$	n/a	n/a	0.937	n/a

*Acquisition continued until a whole-body data set was acquired or until the maximum coverage was reached in the feet-head direction. The number listed is the maximum acquired coverage.

Table 2.1: An overview of scanner parameters and constants used for MR acquisition and reconstruction used in this thesis.

3

Muscle Tissue Segmentation

The second step of the muscle composition analysis chain is finding the region of interest (ROI), *i.e.* muscle tissue segmentation. Segmentation is in this thesis defined as the process of labeling voxels to different muscle compartments. All voxels with the same label belong to a certain muscle compartment, *i.e.* the muscle's *ROI* or *mask*.

Manual definition of the ROI is, as discussed in Chapter 1, a cumbersome, time consuming task. One of the aims of this thesis was therefore to develop an automatic total and regional muscle tissue analysis algorithm. The development of an automatic method was the main aim in Paper I and is also described in detail in Section 3.1. However, the importance of manual definition of muscles can not be neglected. Today, the gold standard is segmentation performed or approved by a human expert, *e.g.* an experienced radiologist or equivalent. Alternative automatic methods therefore still need to be validated in comparison to the manual definitions. Furthermore, automatic methods based on supervised machine learning also need anatomical definitions for training.

Historically it has been hard to rapidly acquire whole-volume data at sufficient resolution due to scanner platform limitations. Furthermore, robust automatic segmentation methods have previously not existed for muscle composition analysis. Therefore, many muscle analyses have been (and often still are) based on cross-sectional definitions in a limited number of slices of the muscles. This thesis mentions in Chapter 1 that whole-volume coverage of the muscles would yield a better precision of the measurement since ambiguity due to non-exact placement of the cross-sectional slices and variation due to anatomical variation in muscle composition throughout the muscle tissue will not be an issue in whole-volume coverage. On the other hand, if a trauma, like a whiplash trauma in the neck, affects the muscles very locally (only at a specific cervical level), a whole-volume approach might hide that finding. Therefore, both cross-sectional segmentation on four axial slices

and whole-volume coverage segmentation were performed for the multifidus muscles.

In total, three different methods for finding the muscle ROI:s were used in this thesis: *Active contours*, using Analyze Version 11.0 (AnalyzeDirect, Overland Park, KS, USA); *Image foresting transform* using a method described by Malmberg *et al.* [48]; and *Multi-atlas segmentation* using the method described in Section 3.1. An overview of the segmentation method used for each of the muscles analyzed in this thesis is presented in Table 3.1.

Region of Interest	**Segmentation Method**		
	Active Contours*	Image Foresting Transform†	Multi-Atlas Segmentation‡
Left multifidus	II	III	
Right multifidus	II	III	
Left abdomen		I§	I
Right abdomen		I§	I
Left arm		I§	I
Right arm		I§	I
Left lower leg		I§	I, III
Right lower leg		I§	I, III
Left anterior thigh		I§	I, III, IV
Right anterior thigh		I§	I, III, IV
Left posterior thigh		I§	I, III, IV
Right posterior thigh		I§	I, III, IV
Left rectus femoris			IV
Right rectus femoris			IV

*Using Analyze (AnalyzeDirect 11.0, Overland Park, KS, USA).
†Using the method presented by Malmberg *et al.* [48].
‡Using the method presented in Section 3.1.
§For creating the atlases.

Table 3.1: An overview of the segmentation algorithm used in the different papers for the 14 different muscle definitions used in this thesis.

An active contour-based algorithm is based on manually outlining the borders of the region of interest, see example in Figure 3.1. The method is very time-consuming and is therefore most often used for a few slices defined using different landmarks, *e.g.* different cervical levels. The method is straightforward but is also sensitive to the placement of the landmarks. With a high variability in the landmarks, the method becomes sensitive to anatomical variations and clinical differences not found.

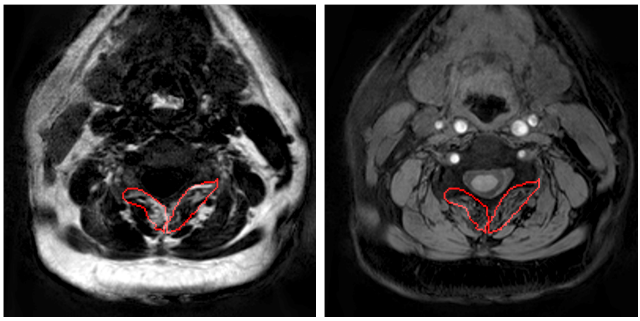

(a) Fat image (b) Water image

Figure 3.1: A cross-section at cervical level C4 of (a) the fat image in which the contour was drawn, and (b) overlaid on the water image.

An approach based on the image foresting transform interactively labels all the data using manually pre-defined pixels or voxels with correct labels, *i.e.* seed points. The algorithm computes the minimal cost path based on the seed-points, and characterizes each pixel/voxel as belonging to the same class as the seed-point with the least cost. The user can thereafter add seed-points and an updated result will be given. The process is repeated until no more seed-points are added. The algorithm can work in a 3D volume, see example in Figure 3.2. The algorithm is one type of semi-automatic segmentation. Hence, it still requires manual interactions in each iteration and for every segmentation.

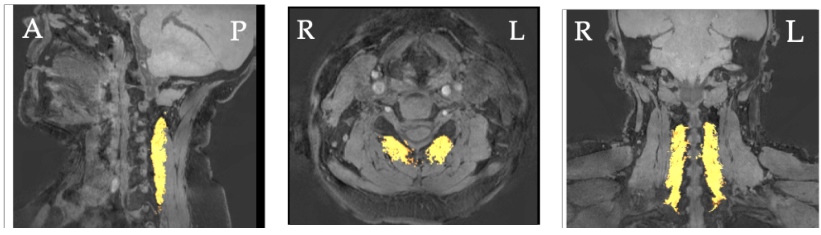

(a) Sagittal slice (b) Axial slice (c) Coronal slice

Figure 3.2: A sagittal (a), an axial (b), and a coronal (c) cross-section of the resulting segmentation using an image foresting based algorithm [48] overlaid on the water image data.

Fully automatic methods still require initial segmentation. It can for example be used for creating atlases in atlas-based methods, see Section 3.1, or ground truth data (reference data) used for deep learning training. The huge efficiency benefit is however, that after initial ground truth data are obtained, the segmentation is fully automated, *i.e.* no further human interaction

is needed. In this thesis, a multi-atlas registration approach was chosen, but several other approaches exist [49].

3.1 Automatic Multi-Atlas Segmentation

A main goal of this thesis and the main aim of Paper I was to develop and evaluate a fully automatic segmentation algorithm for total and regional muscle tissue segmentation using CSE-MRI. The proposed method was divided into the following steps: creation of atlases, non-rigid multi-atlas phase based registration, and lastly muscle tissue region classification using probability voting.

Creation of Atlases

The first important step in multi-atlas segmentation is to have access to a high-quality atlas database. At the starting point of this thesis work, few papers describing muscle tissue segmentation were published. There were even fewer papers published using whole-volume muscle tissue segmentation and none using multi-atlas registration. Therefore, the first step was to create an atlas database. The definition of an atlas in this thesis is a water and fat image pair after a inhomogeneity correction using CIIC [45] together with labeled voxels where different labels correspond to different muscle compartments. The labeled voxels could be individual muscles, *e.g.* rectus femoris or muscle groups, *e.g.* anterior thigh, depending on the purpose. The labels used in this thesis are presented in Table 3.1. An example of an atlas is shown in Fig 3.3. Each muscle or muscle group were manually defined using the semi-automatic image foresting transform segmentation algorithm [48].

Non-Rigid Multi-Atlas Registration

In Figure 3.4, a scheme of the registration procedure is illustrated and also described here in detail. First, one atlas is chosen from the atlas database to be registered onto the target image with the aim to be as similar as possible to the target. The non-rigid registration method, the Morphon [50], was used for the registration. The morphon is an N-dimensional and multi-scale technique in which a dense displacement field is acquired after each iteration. The displacement field is in turn acquired using a phase-based approach where directional quadrature filters are applied and by solving a least square problem the final displacement field is obtained. The final displacement field is then applied to the muscle masks of the atlas and results in automatically generated muscle masks, M_{AUT} of the target. To increase the robustness of the algorithm, not to be dependent on single registration performances, the process is repeated using multiple registrations of different atlases.

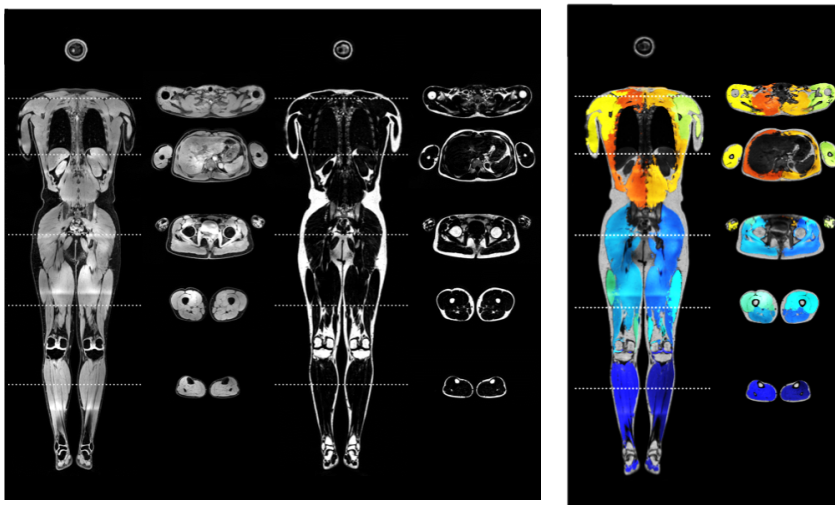

(a) Water-fat separated images (b) Pre-defined labels

Figure 3.3: An example of an atlas acquired at 3 T where (a) shows a coronal slice of the image data, *i.e.* the water and fat separated image pair and (b) shows the 10 pre-defined muscle labels used in Paper I in different colors.

Probability Voting

At this stage, the algorithm has produced N suggestions, where N is the number of atlases used in the multi-atlas registration. The final stage is to obtain one final resulting mask, *i.e.* the M_{AUT}. M_{AUT} is obtained using a concept named probability voting. The different muscle masks resulting from the multi-atlas registrations are first summed and then normalized to range between 0 and 1, creating a so called probability map. The probability map then describes how many of the atlases that agree on a single voxel to belong to a certain muscle region. In Figure 3.5, an example using the results from nine atlases is shown. In the middle, the probability map is shown where dark red equals 1, *i.e.* all the nine atlases agrees on those voxels to be a muscle. Blue instead indicates that none of the atlases agrees on those voxels belonging to a muscle group. Each of the N labeled muscle ROIs yields there own probability map. In Figure 3.5, the whole-body muscle mask was used to illustrate the probability voting.

The last step is to determine the threshold, *i.e.* how many atlases or how many percent of the atlases that needs to agree in order to classify it as a specific muscle or muscle group. The name indicates that a majority of the atlases should agree, but it is not certain that 50% would be the *optimal threshold*. Therefore, this thesis used a method for finding the optimal threshold for this algorithm. That method is presented in detail in Chapter 5. After applying

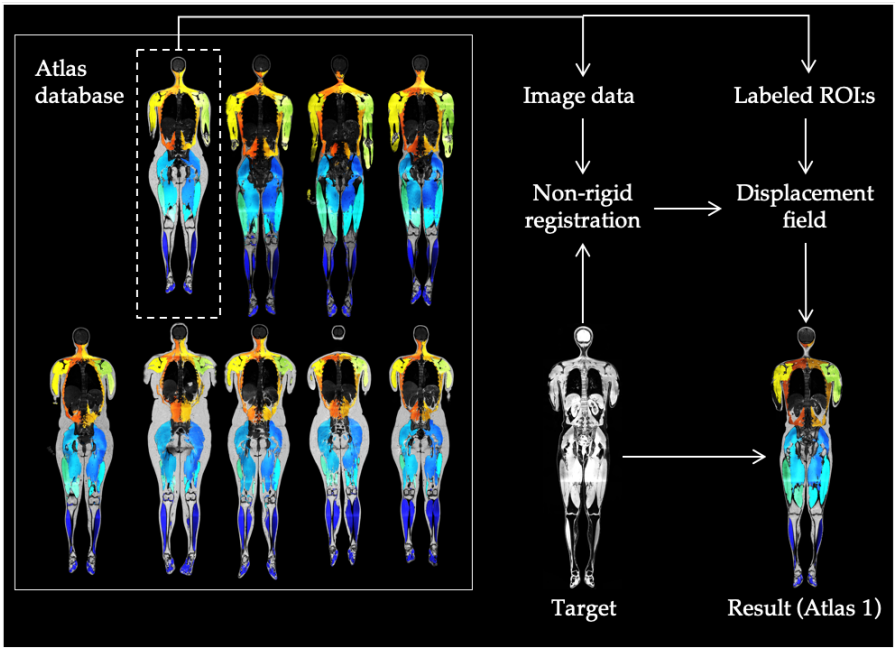

Figure 3.4: An illustration over the automated multi-atlas muscle segmentation algorithm. Each atlas consists of water and fat image volume data together with anatomical information labels, *i.e.* in this image ten different muscle tissue regions. The algorithm starts by taking the image data from one atlas. The image data is non-rigidly registered onto the target volume. The resulting displacement field is used for registering the anatomical labeled masks onto the target volume and an automatic suggestion from the first atlas is achieved. This process can be repeated with different atlases registered on the target image volume.

the chosen threshold, the resulting muscle masks are obtained. See Figure 3.5, to the right, where the different masks are labeled with different colors.

3.2 Supervised Automatic Muscle Tissue Segmentation

Fully automatic segmentation algorithms using input data (*e.g.* atlases), including the algorithm presented in Section 3.1, are based on history, *i.e.* the information available in the input data. This is the case both for registration methods and supervised machine learning techniques, *e.g.* deep learning approaches. Even if multi-atlas registration followed by a voting scheme is more robust than a single atlas registration, it will be challenged by unseen anatomical variations or artifacts in the images, *e.g.* a metal implant.

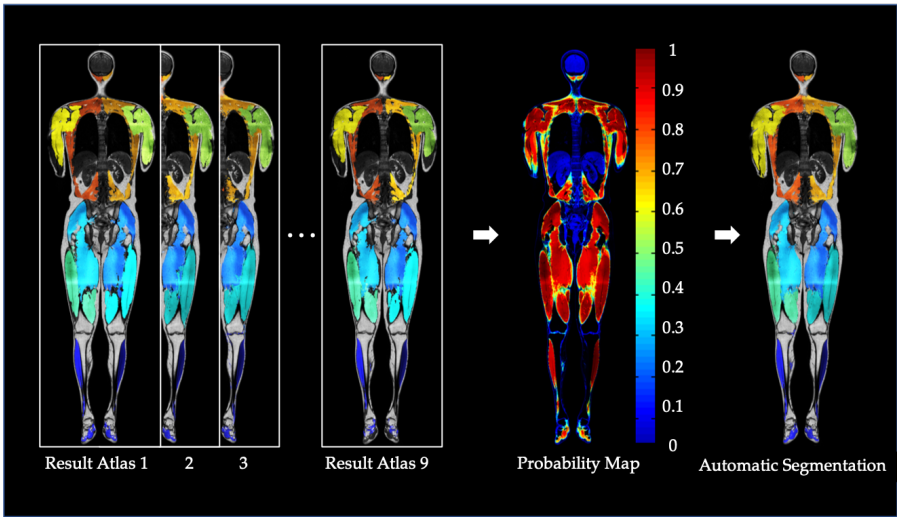

Figure 3.5: Obtaining final muscle masks using multi-atlas registration. First, the suggestions (in this example nine) from the atlas registration step are added and normalized, creating a probability map where 1 (red) means that all atlas suggestions agreed on the specific muscle to be a muscle tissue. Zero (blue) means that no atlas suggested that tissue to be muscle tissue. After probability voting, at a certain threshold determining how many atlases that needs to agree, an automatic segmentation (to the right) is obtained.

One solution to the problem is to have a lot of atlases spanning the anatomical variations followed by a smart selection of the atlases before the probability voting. One smart atlas selection approach was implemented in Paper I where a two step voting scheme was implemented. First, all atlases voted. Then, in the second iteration, only the atlases in which muscle volumes closest to the volumes of the target's muscles from the first iteration voted.

However, even if smart selection of prototypes is utilized or multi-atlas registration with a huge variety in the atlas database is used, it is still valuable to be able to modify the result, if needed. An automatic segmentation with the *ability* to modify the result is a *supervised* automatic segmentation (using the same terminology as Hu *et al.* [51]). The distinction between a supervised automatic method and a semi-automatic method is that the latter requires interactions by the human expert. The supervised automatic methods *allows* for modifications if needed, but the human expert does not *have* to interact. The benefit of a supervised method is that it can be modified if needed. Hence, if quality assurance, including potential modification, is performed by a human expert, the result is gold standard. Therefore, if the atlas database would benefit of being increased, the generated result can become an atlas for future segmentations.

It is not guaranteed that a fully automatic muscle tissue segmentation method is a supervised segmentation method. The presented algorithm presented in Section 3.1 however does allow for supervised automatic muscle tissue segmentation. Since the M_{AUT} is determined after a certain threshold based on a the probability map it is possible to locally change the threshold if needed. For example, an increase of the threshold can be performed if the segmentation leaked into nearby tissue, which was not part of the muscle ROI. Alternatively the threshold can be decreased if part of the muscle is missing. This feature was part of the muscle segmentation used in Paper IV.

4

Quantitative Muscle Volume and Fat Infiltration

The third step of the muscle composition analysis chain is *feature extraction*, *i.e.* quantification of muscle volume and fat infiltration. As described in the previous chapter, a muscle mask, M_{M} was acquired either automatically, M_{AUT}, or manually, M_{MAN}. In this chapter, a method for extracting quantitative information regarding the muscle tissue volume and MFI from M_{M} is presented. Quantification of muscle volume is described in Paper I and is also described in detail in Section 4.1. The extraction of MFI is described in Paper II, III and IV and is also described in detail in Section 4.2.

4.1 Quantification of Muscle Tissue Volume

One straight-forward approach for attaining the volume of the muscle group defined by the binary M_{M} is to count all voxels and multiply it with the volume of each voxel, V_{vox}. However, in order to be a quantitative tool for quantifying a certain compartment, compensation for partial volume effects is needed.

Partial volume effects occur due to the discrete boundary between compartments. Regardless of the resolution, at the border between two different tissue types, there will be voxels that contain signal from both tissue types. One way of illustrating the partial volume effect is to observe the interaction between the water and fat signal in the *op* and *ip* images. In Figure 4.1, the two arrows, A and B, show two places where partial volume effects are visible. A is an example around the border between muscle tissue and subcutaneous fat tissue. B shows the partial volume effects of inter-muscular fat that may be in a posterior muscle group definition. Assuming all confounding factors have been taken into account then $op = abs(f - w)$) meaning that voxels containing equal amount of water and fat protons ($p_w = p_f$), will cancel each other out. For the *ip*-image, voxels containing signal from both fat and the water protons will have an additive effect ($op = abs(f + w)$). Note that chemical shift

op and *ip* images were only used as an example since they have such a visible effect due to the signal being canceled in the *op* image when partial volume effects exists. However, partial volume effects occur in all digital images at the border between different compartments/contrasts.

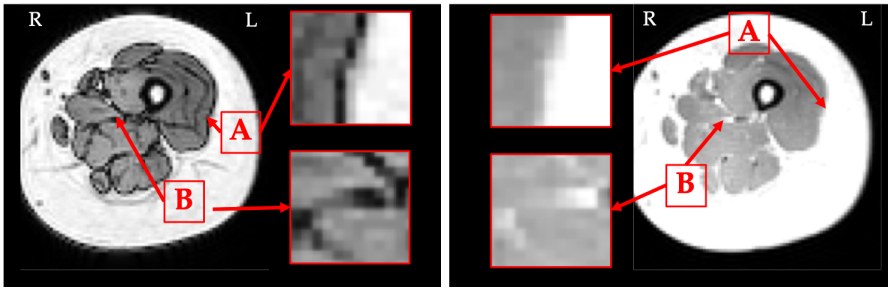

(a) *op* (b) *ip*

Figure 4.1: Illustration of the partial volume effects using: (a) an opposed-phase, *op* image and (b) the corresponding in-phase, *ip* image at a cross-section of the left thigh. The signal in voxels containting equal amounts of water and fat images will darker in (a) since $op = \text{abs}(f - w)$ and remain bright in (b) since $ip = \text{abs}(f + w)$. A and B show two examples in the images. A points at the effect on the border between the muscle tissue and subcutaneous fat. B instead points on the border effect between muscle tissue and inter-muscular adipose tissue.

If correction for partial volume effects is not performed, a bias will be introduced in the volume estimate and this bias will be resolution-dependent [52]. The border between tissues, illustrated with the arrow A in Figure 4.1 will always contain voxels with partial volumes regardless of the resolution why sub-pixel quantification is needed. Also, if no compensation is made for partial volume effects, thin fatty streaks could be lost if the resolution is too low.

Although the example illustrates the partial volume effect in the transition between fat and water, partial volume effects also occur in relation to background and non MRI-visible compartments (such as bone minerals).

Fuzzy Body Tissue Mask

To minimize partial volume effects, and also for removal of noise from voxels outside the body, a *fuzzy* body mask is applied on the image. The term *fuzzy* means that the mask is not binary *i.e.* it contains sub-voxel information. The mask is calculated by first normalizing the water image using CIIC [45], as

was already done with the fat image, see Chapter 2. After that, a binary body mask, M_{body}, is created by

$$\forall \text{voxels}, M_{\text{body}}(\text{vox}) = \begin{cases} 1 & \text{if } f_{\text{RFC}} + w_{\text{RFC}} \geq 0.5 \\ 0 & \text{if } f_{\text{RFC}} + w_{\text{RFC}} < 0.5 \end{cases} \tag{4.1}$$

where vox is a voxel in the $(f_{\text{RFC}} + w_{\text{RFC}})$ image volume. The *fuzzy* body tissue mask, m_{body}, is then calculated by setting the voxels at the border of M_{body} equal to the sum of the quantitative fat image and the normalized water image. This operation also minimizes the contribution of background in the muscle volume estimate.

Muscle Mask Volume

An illustration of M_{M} (acquired either automatically or manually, see Chapter 3) is shown in Figure 4.2. The illustration shows a binary map where all MR visible tissue in the muscle definition is shown.

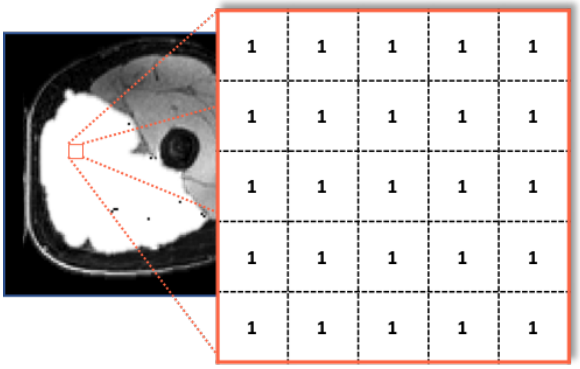

Figure 4.2: An illustration of the left posterior thigh muscle mask overlaid onto a cross-section of the water image. The zoomed area shows the values of the mask in each voxel. In this muscle mask definition no correction for muscle fat infiltration is done.

The mask is binary and each voxel with a specific muscle label has the value 1. The muscle mask volume, $V_{M_{\text{M}}}$ is then calculated by

$$V_{M_{\text{M}}} = \sum_{\forall \text{voxels}} (M_{\text{M}} \cdot m_{\text{body}}) \cdot V_{\text{vox}}, \tag{4.2}$$

where M_{M} is the muscle segmentation (defined automatically, M_{AUT}, or manually, M_{MAN}), m_{body} is the fuzzy body mask, and V_{vox} is the voxel volume. This volume definition calculates all voxels equally within M_{M}. However, this definition of muscle volume also includes fat infiltration and is affected by

partial volume effects at the border to surrounding tissue. V_{M_M} should therefore be used if only the complete volume is of interest and not if the volume of non-fatty tissue is more interesting. If removal of larger fatty streaks is of interest the *fat-free muscle volume* should be used instead.

Fat-Free Muscle Volume

The fat free muscle mask, M_{FF} is defined by

$$M_{FF} = M_M(f_{RFC} < 0.5), \tag{4.3}$$

where f_{RFC} is the calibrated fat signal, described by Equation 2.12. An illustration of the mask is shown in Figure 4.3. The mask is still binary but larger fatty streaks are removed from the mask definition, as can be seen in the zoomed area.

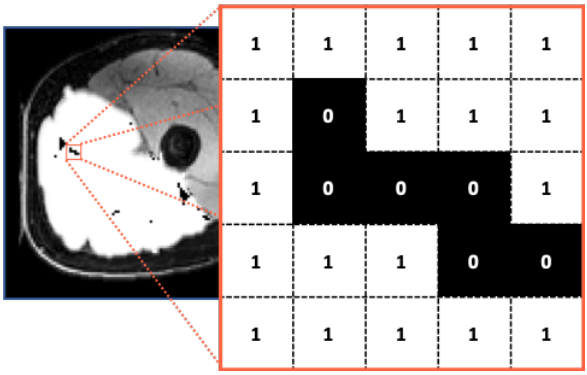

Figure 4.3: An illustration of the left posterior thigh fat free muscle mask (M_{FF}) overlaid onto a cross-section of the water image. The zoomed area shows the values of the M_{FF} in each voxel. In this muscle mask definition, no correction for diffuse MFI is done.

The fat free muscle volume, $V_{M_{FF}}$ is defined by

$$V_{M_{FF}} = \sum_{\forall \text{voxels}} (M_{FF} \cdot m_{body}) \cdot V_{vox}. \tag{4.4}$$

where m_{body} is the fuzzy body mask and V_{vox} is the voxel volume. This muscle volume definition removes large inter-muscular fatty compartments that otherwise would contribute to the signal when multiple individual muscles are analyzed as a group, *i.e.* the left anterior thigh. However, the definition is limited by not being able to compensate for diffuse fat infiltration and not being able to correct for partial volume effects in the borders between fat and water. If removal of all fat signal is of interest, the *lean muscle volume* should be used.

Lean Muscle Volume

The lean muscle mask is defined by

$$M_{\mathrm{L}} = M_{\mathrm{M}}(1 - f_{\mathrm{RFC}}), \tag{4.5}$$

where f_{RFC} is the calibrated fat signal, decribed by Equation 2.12. An illustration on the resulting (fuzzy) mask, M_{L}, is shown in Figure 4.4. Observe that the mask is not a binary definition but instead represents the *lean tissue* concentration of each voxel. Due to noise in the f_{RFC} image, some values are higher than 1, meaning that the fat signal is less than 0 in the voxel. However, removing negative values due to noise would bias the result and *i.e.* f_{RFC} would be overestimated since the positive noise contribution cannot be estimated and adjusted for. Hence, the lean volume would be underestimated. Assuming Gaussian noise and large enough amount of voxels, the final volume estimate is unbiased.

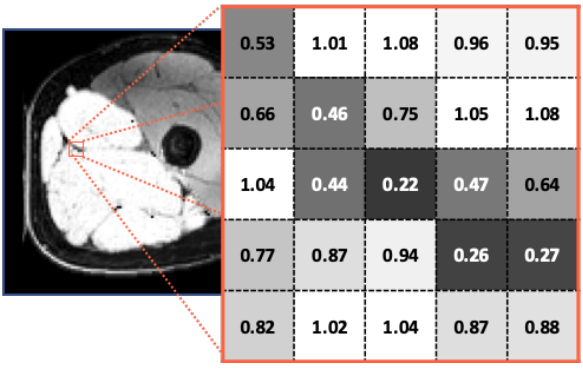

Figure 4.4: An illustration of the fuzzy lean tissue mask (M_{L}) definition of the left posterior thigh overlaid onto a cross-section of the water image. The zoomed area shows the values of the M_{L} in each voxel.

The lean muscle volume, $V_{M_{\mathrm{L}}}$ is calculated as

$$V_{M_{\mathrm{L}}} = \sum_{\forall \mathrm{voxels}} (M_{\mathrm{L}} \cdot m_{\mathrm{body}}) \cdot V_{\mathrm{vox}}, \tag{4.6}$$

where m_{body} is the fuzzy body mask and V_{vox} is the voxel volume. The volume only measures the lean muscle tissue without any influence from either partial volume effects or fat.

However, as mention in Chapter 1, it is of high clinical interest to also acquire a quantitative MFI estimation. This will be discussed in detail in the next section.

4.2 Muscle Fat Infiltration

A straight-forward way of quantifying fat in muscles is to calculate the fat volume of M_{M} as $V_f(M_{\mathrm{M}}) = \sum_{\forall \mathrm{voxels}} f_{\mathrm{RFC}} \cdot M_{\mathrm{M}}$. However, this definition has limitations; First, the estimate will be sensitive to errors in the segmentation, *e.g.* leakage of the mask into subcutaneous fat, which would overestimate the result; Second, the fat infiltration will be overestimated since it includes larger inter-muscular streaks if muscle groups are analyzed and; Third, no relation is made to the size of the muscle itself, making the volume of fat inside the muscle difficult to interpret clinically.

Therefore, it is more appropriate to calculate the fraction of fat inside the muscle ROI. Furthermore, by calculating the fraction using the fat free muscle mask, M_{FF}, potential contributions of leakage in the subcutaneous fat are minimized. The fat-referenced muscle fat infiltration can then be defined by

$$\mathrm{MFI}_{f_{\mathrm{RFC}}} = \frac{\sum_{\forall \mathrm{voxels}} (f_{\mathrm{RFC}} \cdot M_{\mathrm{FF}})}{\sum_{\forall \mathrm{voxels}} (M_{\mathrm{FF}})}. \tag{4.7}$$

Note that, by the definition of f_{RFC} described by Equations 2.9 and 2.12, this fraction should be interpreted as the AT-equivalent fat concentration (Equation 2.9) or, in other word, the amount of fat of the muscle in relation to the amount of fat in pure adipose tissue (see Equation 2.12). To relate the MFI-estimate to the total number of (MR-visible) protons in the ROI, $\mathrm{MFI}_{f_{RFC}}$ can be converted to the PDFF by scaling it with the PDFF of the reference signal ($\mathrm{PDFF}_{\mathrm{ref}} = \mathrm{PDFF}_{\mathrm{AT}}$), see Equation 2.14. The PDFF equivalent MFI estimate is defined by

$$\mathrm{MFI}_{\mathrm{PDFF}} = \mathrm{PDFF}_{\mathrm{AT}} \cdot \frac{\sum_{\forall \mathrm{voxels}} f_{\mathrm{RFC}} \cdot M_{\mathrm{FF}}}{\sum_{\forall \mathrm{voxels}} (M_{\mathrm{FF}})}. \tag{4.8}$$

In Equation 4.8, the volume of MR-invisible protons in M_{FF} is assumed to be equal to the volume of MR-invisible protons of the fat reference voxels used for the fat calibration [24]. Furthermore, PDFF of AT is assumed to be constant between individuals. In this thesis, the PDFF of AT was estimated to be $\mathrm{PDFF}_{\mathrm{AT}} = 0.937$. The estimate is based on unpublished data from 95 participants where PDFF in the subcutaneous AT was measured. $\mathrm{PDFF}_{\mathrm{AT}} = 0.937$ has also been used in other reports validating the test-retest performance of this estimate [53].

Both Equations 4.7 and 4.8 require an accurate calibration of f_{RFC} in order to be a quantitative measurement. f_{RFC} has been proven to be very robust [24] but there are situations where it could be challenged. One pre-requisite for the method to work is that the algorithm finds pure AT voxels to be used as calibration reference close to the ROI. If the resolution is too low it can be difficult to find those voxels without influence of other tissue compartments, especially if the subject is lean and the target area is problematic. Problematic

areas are *e.g.* where large inhomogeneities are present in combination with a large distance to pure AT voxels.

In circumstances where f_{RFC} is challenging to obtain, an alternative is to calculate the MFI as the fat fraction (FF), by relating the fat signal to the total signal ($f + w$) as done in PDFF, see Equation 2.8. The FF of a ROI is calculated by

$$\text{FF} = \frac{\sum_{\forall \text{voxels}}(s_f)}{\sum_{\forall \text{voxels}}(s_f + s_w)}, \tag{4.9}$$

where s_f and s_w is the non-calibrated fat and water signal in a voxel. However, since the denominator is co-located with the numerator, the equation becomes self-calibrating and insensitive to inhomogeneity. Consideration must however be taken regarding potential confounding factors before using FF, *e.g.* its sensitivity to T_1-bias.

5

Method Evaluation

Chapters 2 – 4 present the three first links in the muscle composition analysis chain. Since the links affect each other, the evaluation performed on the muscle composition method is presented as a whole in this chapter. The data analysis in clinical studies, link four, is presented in Chapter 6. The method evaluation was performed mainly in Paper I and in Paper IV using three different cohorts, presented in Table 5.1. The threshold optimization is presented in Section 5.2.

In this thesis, accuracy and precision were evaluated for muscle volume and fat infiltration. In Paper I, accuracy of automatic muscle segmentation was investigated, which is also summarized in Section 5.3. Furthermore, in Paper I, the precision when using different field strengths and image resolutions was also investigated and the results are summarized in Section 5.4. In Paper IV, the accuracy and precision of acquisitions with different flip angles were investigated and the results are summarized in Section 5.5 and Section 5.6.

5.1 Cohorts

In total, three different cohorts were used in the method evaluation:

- Cohort C_{I1} was used in Paper I for atlas creation, evaluating accuracy of automatic segmentation compared to manual segmentation, and evaluating precision when changing scanner field strength and changing image resolution.
- Cohort C_{I2} was used in Paper I for validation used for evaluating the performance of the algorithm on a cohort not included in the atlas database.
- Cohort C_{IV} was used in Paper IV to investigate the potential impact in accuracy and precision when changing flip angle.

A demographic summary of the three different cohorts is presented in Table 5.1 and also in detail in Paper I and Paper IV.

	C_{I1}	C_{I2}	C_{IV}
Participants (n)	10	11	40
Women (men) (n)	6 (4)	7 (5)	40 (0)
Age (y)	25±2 (21–29)	44±7 (33–54)	56±6 (45–70)
BMI (kg/m^2)	24±4 (20–32)	26±4 (20–32)	27±4 (19–39)

Table 5.1: Demographic data summary of the three different cohorts that were used in the method evaluation of the muscle composition analysis algorithm. BMI stands for body mass index. Age and BMI are presented as: mean±sd (range).

5.2 Threshold Optimization

One part of an automatic multi-atlas registration algorithm is to determine how many atlases that need to agree on a voxel belonging to a certain ROI, *i.e.* a certain tissue type. As also mentioned in Chapter 3, the terminology *probability voting* does not imply that the threshold *has* to be when more than half of the atlases agree. Therefore, Paper I included finding the *optimal threshold*. The optimal threshold was acquired for all 10 muscle groups separately.

The data from the 10 participants from cohort C_{I1} were used for the threshold optimization. First, the manually created masks, M_{MAN} (defined in Chapter 3) were used as reference. The optimization was made for the 1.5 T and 3 T acquired data separately.

A leave-one-out approach was used for the threshold optimization. Leave-one-out in multi-atlas registration means that one of the (in this case 10) data sets is used as a target (with its manually defined masks being considered as the ground truth reference), while the rest of the data are used as atlases. This is repeated for all the data sets in the cohort. When finished, all of the data sets have been used as target once. In this evaluation it meant that each of 10 data sets resulted in nine automatically defined segmentation regions for each of the 10 different muscle groups.

In the next step, M_{AUT} was generated for each threshold. A threshold equal to 1 means that the mask is defined at all voxels in the targeting data volume where at least 1 of the atlases defined it at the specific muscle region of interest. The Dice similarity coefficient (DSC) [54] was used to compare the similarity between the reference, M_{MAN}, and for each of the two automatic

generated masks M_{AUT} and M_{FF} (defined in Chapter 4). The DSC is defined as

$$\mathrm{DSC} = \frac{2 \mid A \cap B \mid}{\mid A \mid + \mid B \mid}. \tag{5.1}$$

where A and B are the logical masks to be compared to each other. The DSC was therefore not used on M_{L} since it is not a logical mask.

In Figure 5.1, graps over the DSC of M_{FF} compared to M_{MAN} are shown (at 1.5 T) for two of the muscle groups (left anterior thigh in 5.1a and 5.1b and right abdomen in 5.1c and 5.1d). All 10 targets follows the same patterns of having a peak around threshold 3-5 and then starting to decrease again. There is not any distinct difference in the shape of the curve for the two muscle groups except that right abdomen has a lower DSC using higher thresholds.

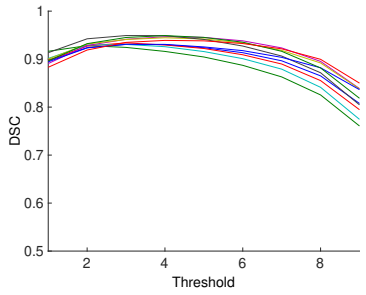

(a) All DSC - left anterior thigh

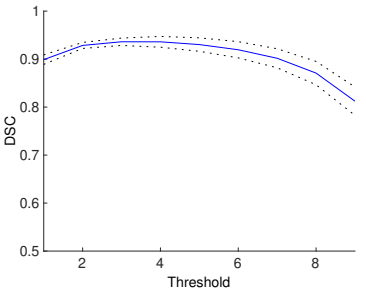

(b) Mean DSC - left anterior thigh

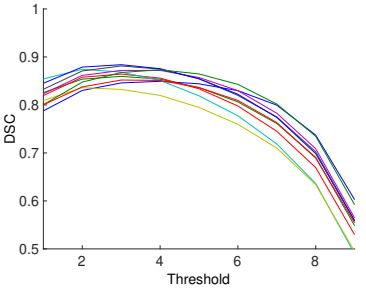

(c) All DSC - right abdomen

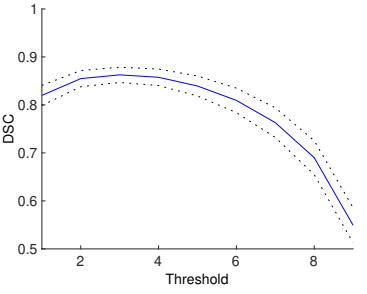

(d) Mean DSC - right abdomen

Figure 5.1: Showing the dice similarity coefficient (DSC) changes with different threshold values for all individuals in left anterior thigh (a) and right abdomen (c) as well as the mean DSC ± sd in left anterior thigh (b) right abdomen (d).

In Table 5.2, the highest mean DSC, ± sd, and its corresponding threshold (th), calculated both for M_{M} and M_{FF}, are presented for both field strengths.

Muscle Group	Field strength	M_{M} th	M_{M} DSC	M_{FF} th	M_{FF} DSC
Left lower leg	1.5 T	4	0.92 (0.01)	3	0.94 (0.01)
	3 T	4	0.92 (0.02)	4	0.94 (0.02)
Right lower leg	1.5 T	4	0.92 (0.01)	3	0.94 (0.01)
	3 T	4	0.91 (0.02)	3	0.93 (0.01)
Left posterior thigh	1.5 T	4	0.89 (0.02)	3	0.93 (0.01)
	3 T	5	0.90 (0.01)	4	0.93 (0.01)
Right posterior thigh	1.5 T	5	0.90 (0.01)	4	0.93 (0.01)
	3 T	4	0.89 (0.02)	4	0.92 (0.02)
Left anterior thigh	1.5 T	4	0.91 (0.01)	3	0.94 (0.01)
	3 T	4	0.91 (0.01)	4	0.93 (0.01)
Right anterior thigh	1.5 T	4	0.91 (0.01)	4	0.94 (0.01)
	3 T	5	0.92 (0.02)	4	0.94 (0.02)
Left abdomen	1.5 T	4	0.83 (0.03)	3	0.87 (0.02)
	3 T	4	0.79 (0.02)	4	0.84 (0.03)
Right abdomen	1.5 T	4	0.82 (0.03)	3	0.86 (0.02)
	3 T	4	0.78 (0.03)	3	0.82 (0.02)
Left arm	1.5 T	4	0.79 (0.05)	3	0.83 (0.05)
	3 T	4	0.85 (0.03)	3	0.90 (0.02)
Right arm	1.5 T	4	0.80 (0.04)	3	0.85 (0.02)
	3 T	4	0.85 (0.04)	3	0.90 (0.02)

Table 5.2: Table over the number of atlases (of total 9) that gave the highest dice index for the 10 different muscle groups, evaluated on the two binary masks M_{M} and M_{FF}. The mean standard deviation of the ten different individuals is also presented for both M_{M} and M_{FF}.

The mean DSC was higher for M_{FF} than for M_{AUT} in all muscle groups for both field strengths. The final optimal thresholds were therefore chosen from the threshold of the highest mean M_{FF}. Worth noting is also that the optimal thresholds for M_{FF} were less than or equal to M_{M} for all muscle groups. Hence, less atlases needed to agree in order to classify it as muscle tissue.

When the optimal threshold was evaluated and chosen, the next step was to evaluate the automatic results compared to the manual definitions.

5.3 Accuracy of Muscle Volume

The accuracy of the three different automatic muscle volumes compared to manual segmentation was thoroughly evaluated in Paper I. In this section, the result from Paper I is summarized using only a subset of the muscle volumes analyzed in Paper I. For a full presentation of all results, see Table 1–4 in Paper I.

In this thesis, three different alternatives for acquiring muscle volume are presented. In figure 5.2, the resulting volumes (in liters) acquired for the three different volume estimates $V_{M_{\mathrm{M}}}$, $V_{M_{\mathrm{FF}}}$ and $V_{M_{\mathrm{L}}}$ are shown for left anterior thigh, right abdomen and whole-body when using cohort C_{I1} (Table 5.1). The results are illustrated for both the 1.5 T (left column) and 3 T (right column).

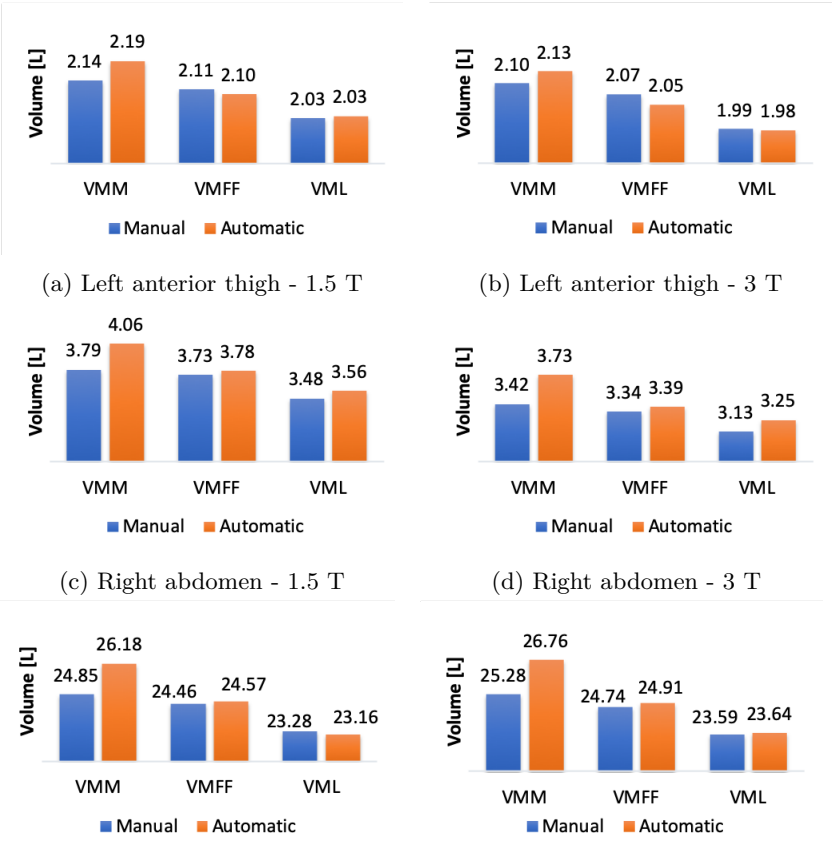

(a) Left anterior thigh - 1.5 T

(b) Left anterior thigh - 3 T

(c) Right abdomen - 1.5 T

(d) Right abdomen - 3 T

(e) Whole-body - 1.5 T

(f) Whole-body - 3 T

Figure 5.2: The mean muscle volumes in liter for the three different muscle volume estimates $V_{M_{\mathrm{M}}}$, $V_{M_{\mathrm{FF}}}$ and $V_{M_{\mathrm{L}}}$ acquired both manually and automatically at two different field strength (1.5 T and 3 T). The top row ((a) and (b)) shows the volumes for the left anterior thigh at 1.5 T and 3 T respectively. The middle row ((c) and (d)) shows the volumes for the right abdomen at 1.5 T and 3 T respectively. The bottom row ((e) and (f)) shows the volumes for the whole-body at 1.5 T and 3 T respectively.

Figure 5.2 shows that the automatic results overestimates the volume compared to manual segmentation for $V_{M_{\mathrm{M}}}$. This is because the optimal threshold was chosen for using M_{FF} and as mentioned earlier, the threshold was lower for M_{FF} than for M_{M}. Therefore, M_{AUT} can leak into subcutaneous fat without influencing the result since subcutaneous fat voxels are removed from the $V_{M_{\mathrm{FF}}}$ definition (Equation 4.4).

The volume estimate was lower for $V_{M_{\mathrm{FF}}}$ compared to $V_{M_{\mathrm{M}}}$ for the automatic results for all muscle groups at both field strengths. The manual segmentation did not differ much. M_{L} gave the smallest estimated muscle volumes for both manual and automatic definitions, which is expected since all diffuse fat infiltration was removed, see Equation 4.6.

Since the threshold optimization was performed on the M_{FF} mask the results that follows will be shown using the $V_{M_{\mathrm{FF}}}$ volumes.

The delta volumes (manual - automatic) and the 95% limits of agreement were also calculated for all muscle groups in order to detect a potential bias between field strengths. Furthermore, the C_{I2} cohort was used for validation in order to detect a potential overtraining of the algorithm since it was optimized using a leave-one-out approach on young, mostly lean, and healthy volunteers. An illustration of the delta volume for left anterior thigh, right abdomen and whole-body are shown in Figure 5.3, where the whiskers illustrate the 95% limits of agreement.

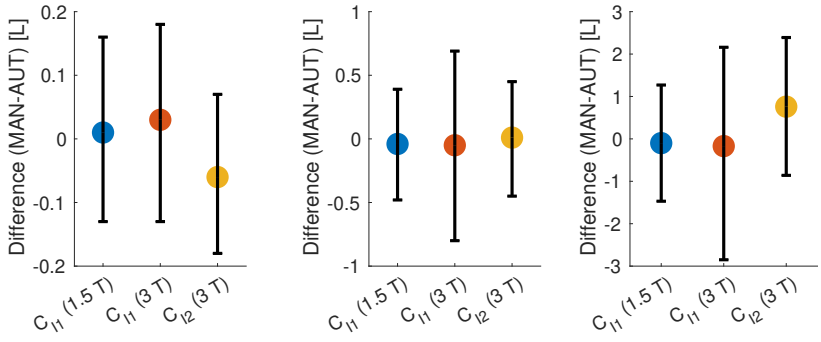

(a) Left anterior thigh (b) Right abdomen (c) Whole-body

Figure 5.3: The mean delta volumes (manual-automatic) for 10 healthy volunteers both at 1.5 T (blue circle) and 3.0 T (orange circle) and 11 additional volunteers used for validation at 3 T (yellow circle). The whiskers illustrate the 95% limits of agreement. The illustration shows the result for left anterior thigh (5.3a), right abdomen (5.3b) and whole-body (5.3c).

Note that the scales on the y-axes in Figure 5.3 differ. Furthermore, the mean volumes of the different muscle groups are also different (mean volume of: left anterior thigh: 2.09 L, right abdomen 3.56 L and whole-body 24.97 L).

See also Figure 5.4 for the coefficient of variation between automatic and manual segmentation using the validation cohort, C_{I2}. Figure 5.3 shows a good agreement between manual and automatic results. There is no detectable bias between the different cohorts and there is no significant differences between the limits of agreement.

Accuracy on Validation Data

Since the atlases used in this training also were used for threshold optimization, 11 additional volunteers were used for validation. In Figure 5.4, an illustration of the result from one target is illustrated with the different muscle groups labeled with different colors. Furthermore, for each muscle, the mean ± sd coefficient of variation for each muscle group is shown for the validation data set C_{I2}.

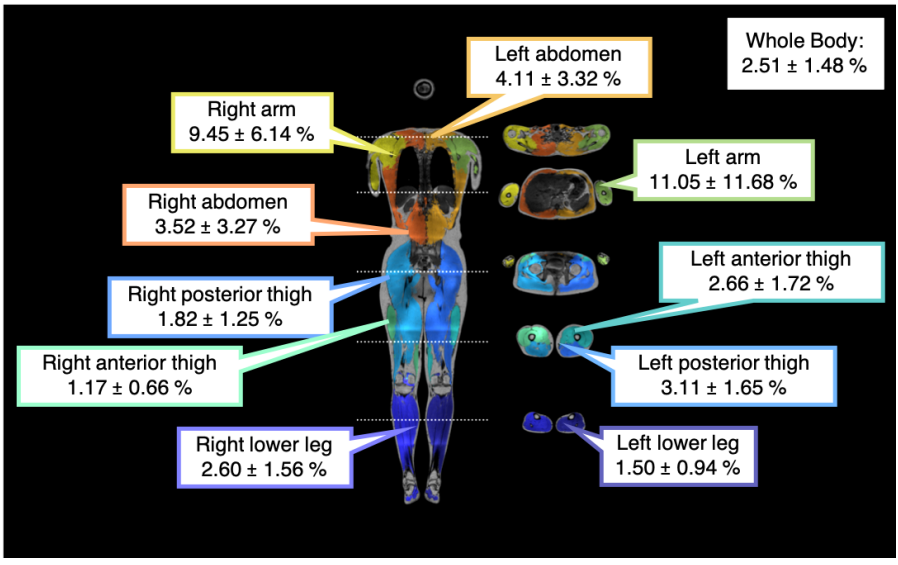

Figure 5.4: The coefficient of variation (mea ± sd) using a validation data set (not used as atlases or threshold optimization) when comparing automatic with manual segmentation. The illustration shows the resulting mask for each muscle group for one data set in the cohort where the different muscle groups are labeled with different colors.

The result shows good agreement with manual segmentation, except for the arms. The coefficient of variation was around 3% or lower for the six leg muscle groups and the whole-body. The abdomen was slightly higher at 4%. The arms are difficult to fit within the FOV for larger individuals, and the image quality is affected in the outer parts of FOV.

The coefficient of variation was complemented with calculating the intraclass correlation (ICC), which was higher than 0.97 (with 95% confidence interval ranging from 0.66-1.00) in all muscle groups except for the arms.

A higher variability was observed in the upper part of the body than in the lower part of the body when investigating muscle volume. This was also observed by Wald *et al.* who also investigated methods for whole-body quantification [21]. Arm placement is especially challenging. In the 1.5 T acquisition in Paper I, the arm-positioning over head lead to too many degrees of freedom between the atlases and targets. In the 3 T protocol the arms were instead positioned alongside the body. In this study 8 of 10 of the participants were lean, *i.e.* the arms fitted the FOV. However, for the larger participants, the arms were not fully included in the FOV. Also, in a study by Thomas *et al.* where a wide bore scanner was used, a higher variability was observed in the arms [55]. In that study, however, the participants were larger. Furthermore, scanner inhomogeneities are more prominent further out from isocenter which might influence the variability.

5.4 Precision of Muscle Volume

The precision of muscle volume was in this thesis evaluated by investigating the reproducibility of the estimate, specifically to test how the precision changes using two different field strengths. Furthermore, the voxel dimensions for the two acquired volumes were half in each direction. Hence, this experiment also investigated the effect of an eight-fold resolution difference.

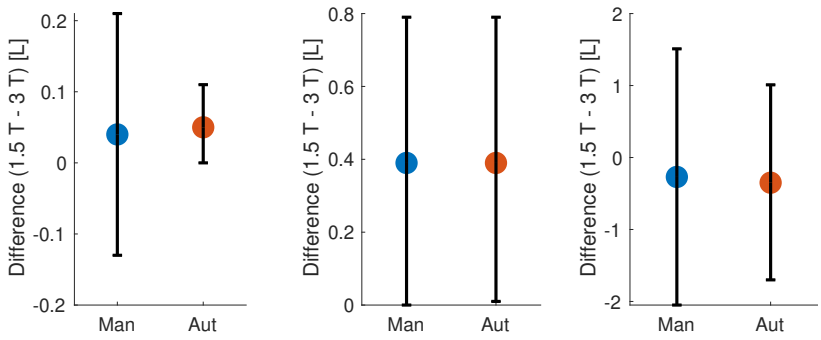

(a) Left anterior Thigh (b) Right abdomen (c) Whole-body

Figure 5.5: The mean delta volumes (1.5 T - 3 T) for 10 healthy volunteers acquired both using manual segmentation (blue circle) and automatic segmentation (orange circle). The whiskers illustrate the 95% limits of agreement. The illustration shows the result for left anterior thigh (5.5a), right abdomen (5.5b) and whole-body (5.5c).

There is a high agreement between the mean difference (1.5 T - 3 T) volumes for the manual segmentation and the automatic segmentation. For the abdomen, a slight trend towards acquiring higher volumes at 1.5 T is observed. Another trend is that the 95% limits of agreement is slightly narrower for many of the muscle groups compared to manual (see also Paper I for additional muscle groups). The automatic results are at least as precise as manual segmentation and the quantitative method is robust to field strength changes as well as the large resolution difference.

5.5 Accuracy of Fat Infiltration

The accuracy evaluation of the two different MFI estimates using a 5° and 10° flip angle is presented in detail in Paper IV and is also summarized in this section. It is not straight-forward to test the accuracy for MFI. Today, the gold standard for acquiring fat infiltration in organs, including muscles, is by biopsy or spectroscopy. Both methods are limited by the small sample size analyzed. Therefore it is not a well suited comparison for whole muscle volume composition analysis where there will be anatomical variances.

In Paper IV, the accuracy was evaluated by investigating the mean MFI_{PDFF} for the two flip angles, 5° and 10°. If the data are affected by T_1-bias, the mean MFI_{PDFF} will be higher using a 10° flip angle, see Figure 5.6. For comparison, the mean FF was also presented to illustrate the effect on data that are affected by T_1-bias. Furthermore, to see the effect of anatomical variance, the mean MFI_{PDFF} and the mean FF were acquired for whole volume and the middle slice (along the feet-head direction).

Although the potential T_1-bias was not compared to *true* PDFF, MFI_{PDFF} was not notably affected by the increase in flip angle. Furthermore, MFI based on FF had a higher mean MFI for all muscles compared to MFI_{PDFF} already at 5°, which could be due to T_1-bias. This implies that MFI_{PDFF} was robust to changes in flip angles between 5° and 10°.

5.6 Precision of Fat Infiltration

The precision evaluation for the two MFI estimates at both 5° and 10° flip angles is presented in detail in Paper IV and is summarized in this section. For both flip angles, two data sets were acquired for each participant (where the participants left the scanner room between the acquisitions). As for evaluating the accuracy, the precision was measured on both the whole volume and the middle slice and FF was used as comparison to MFI_{PDFF}.

In this thesis, the precision of changing flip angle was evaluated by investigating the *repeatability* of the measurement. The repeatability was tested using the within-subject standard deviation s_w (when number of observations

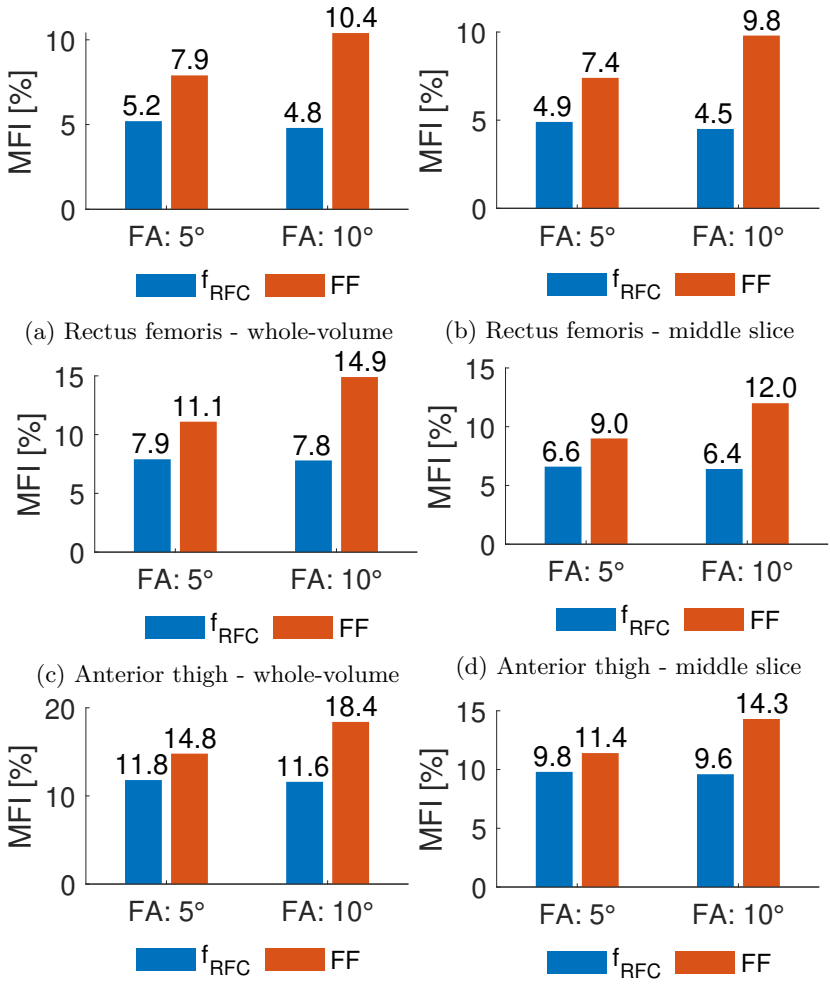

(a) Rectus femoris - whole-volume

(b) Rectus femoris - middle slice

(c) Anterior thigh - whole-volume

(d) Anterior thigh - middle slice

(e) Posterior thigh - whole-volume

(f) Posterior thigh - middle slice

Figure 5.6: The mean muscle fat infiltration using two flip angles, 5° and 10°. Both whole volume (left) and middle slice (right) are presented. f_{RFC} is calculated by Equation 4.8 and FF by a slightly modified version of Equation 4.9 where FF is used as mask to ensure the same ROI in comparing the two measurement.

for each individual is two) calculated by

$$s_w = \sqrt{\frac{\sum_i d_i^2}{2n}} \tag{5.2}$$

where d is the difference between the observations of individual i and n is the total number of individuals. However, to be able to compare s_w between dif-

ferent methods, the magnitude of the estimates must be equal. Since FF was used for comparison and the magnitude of the estimate was higher (probably because of T_1-bias) the within-subject coefficient of variance (wCV) was also analyzed. The wCV is calculated by

$$w\text{CV} = \frac{s_w}{m} \tag{5.3}$$

where m is the mean MFI estimate. Figure 5.7 shows the wCV for the averaged left and right side of the muscle groups. For details about the statistical measures, see Table 2 in Paper IV.

There were no large differences between flip angles or type of MFI measurement in terms of repeatability. A few other findings can however be observed by looking at Figure 5.7. First, the wCV is much higher for a middle slice measurement compared to a whole-body estimate. Second, the wCV is a sensitive measurement when the mean is close to zero. In combination with a small sample size not acquired at the exact same area, as for the middle slice in rectus femoris, the measurement showed a higher variation.

Since a higher flip angle should improve the SNR, an investigation regarding the noise characteristics was also made in Paper IV. To isolate the effect due to noise, histograms of the fat distributions in the voxels were analyzed based on the full width at half maximum (FWHM) estimate. The histograms of the anterior and posterior thigh are shown in Figure 5.8 where the horizontal lines are the FWHM. The histograms are created based on both a whole-body measurement and the middle slice of the measurement.

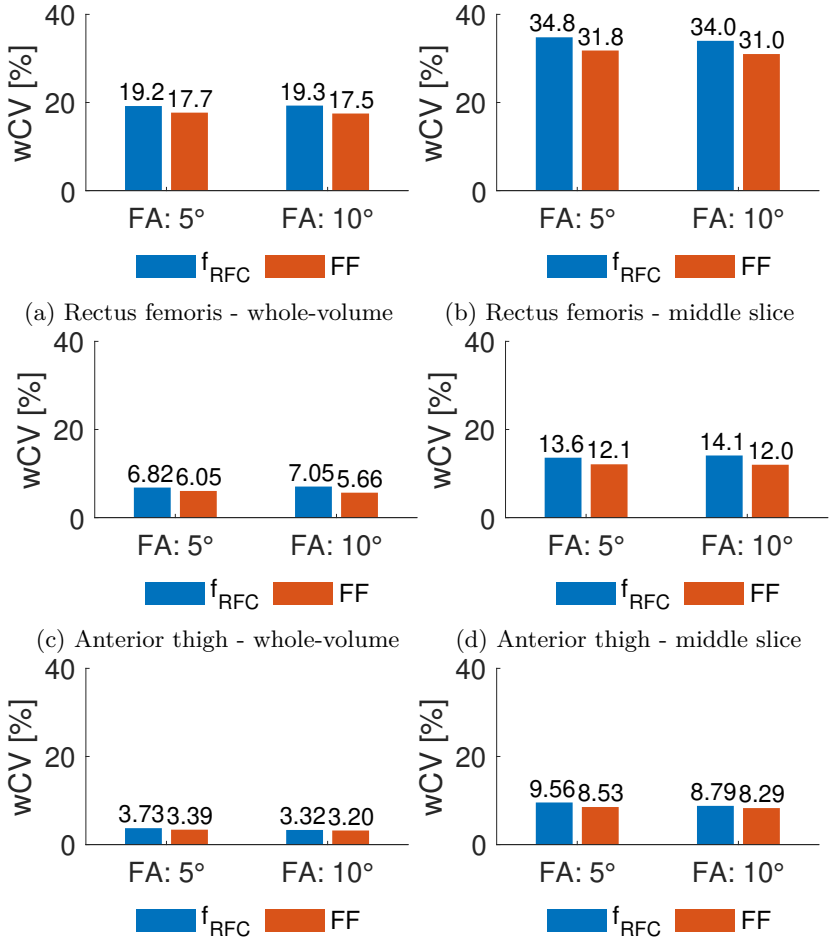

(a) Rectus femoris - whole-volume

(b) Rectus femoris - middle slice

(c) Anterior thigh - whole-volume

(d) Anterior thigh - middle slice

(e) Posterior thigh - whole-volume

(f) Posterior thigh - middle slice

Figure 5.7: The within-subject coefficient of variation comparing two flip angles (5° and 10°) using the fat-referenced MFI estimate (Equation 4.8). FF, used for comparison, is calculated by a slightly modified version of Equation 4.9 where M_{FF} is used as mask to ensure the same ROI in comparing the two measurement. This is illustrated both for whole-volume acquisition and using the middle slice.

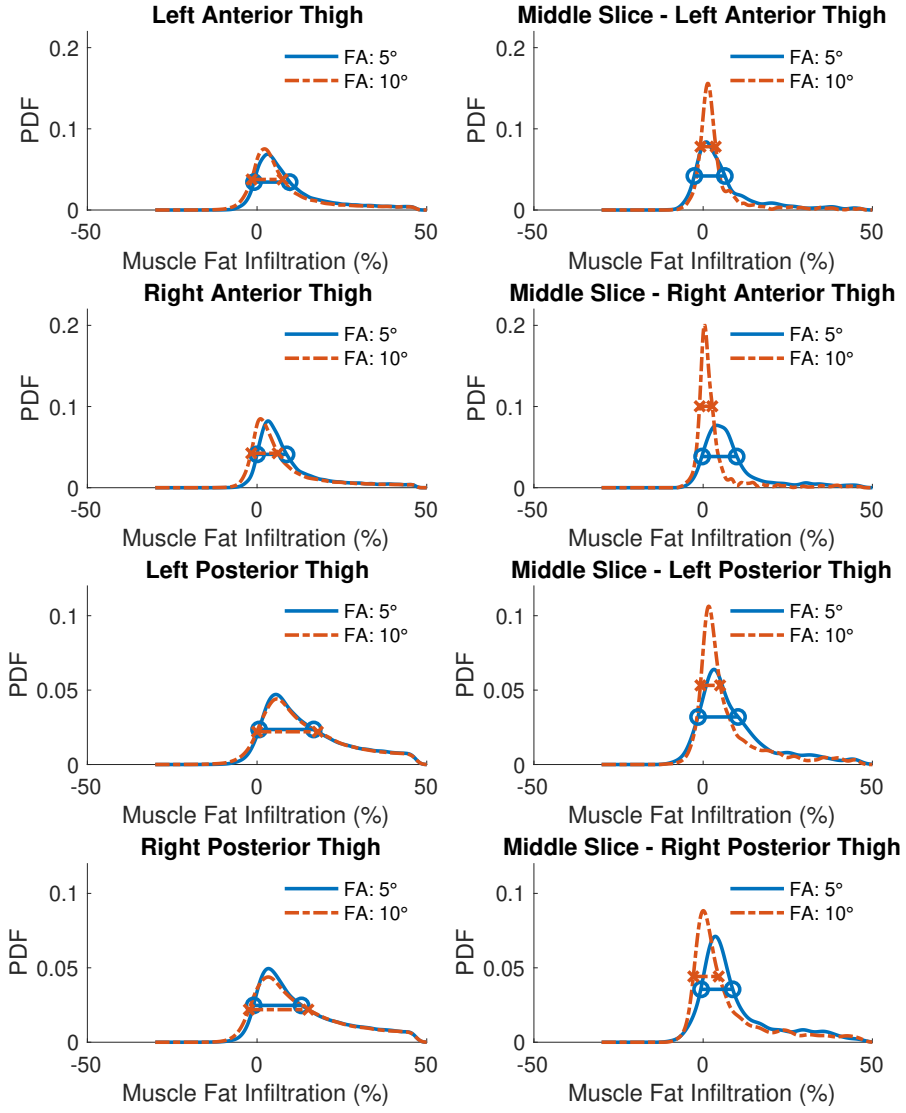

Figure 5.8: The histogram where the fat-referenced MFI for each voxel is anlayzed. PDF is the probability density function.

6

Body Composition Analysis in Clinical Studies

The last step in a body composition analysis chain is the data analysis.

Even though changes in muscle composition have been related to several diseases and syndromes, as mentioned in Chapter 1, questions remain on causes and potential effects of rehabilitation programs. The addition of effective quantitative methods for muscle data analysis could help in investigating causes, diagnosis and potential effects of rehabilitation. The method presented in this chapter can be applied for investigating several syndromes and disorders.

In this thesis, the clinical focus was in patients with chronic ($\geq$ 6 months since injury) WAD. Both small deep neck muscles and whole-body were analyzed to investigate muscle fat infiltration in relation to self-reported neck disability in a case-control study, presented in Section 6.1. Section 6.2 presents a short summary of other clinical studies where the presented muscle composition method has been applied. Those studies were however not part of this thesis.

6.1 Whiplash-Associated Disorders

A whiplash injury is defined by the Quebec Task Force (QTF) [56] as:

> "An acceleration-deceleration mechanism of energy transfers to the neck. It may result from rear-end or side-impact motor vehicle collisions, but can also occur during diving or other activities or mishaps. The impact may result in bony or soft tissue injuries (whiplash injury), which in turn may lead to a variety of clinical manifestations, referred to as whiplash associated disorders (WAD)."

The annual incidence for whiplash injuries is 200-300 cases per 100 000 individuals [57, 58] and, as previously mentioned in Chapter 1, approximately

half of the individuals that get a motor-vehicle related whiplash injury will not fully recover [15]. The symptoms associated with a whiplash injury are both physical (neck pain, headache, radiating arm pain, visual disturbance, dizziness) and psychological (anxiety and depression) [15, 59, 60].

The QTF proposed a five-grade scale to classify severeness of a whiplash injury [56]. The different grades are defined as:

- **Grade 0** No complaint of neck pain. No physical signs.
- **Grade I** Neck pain, stiffness or tenderness only. No physical signs.
- **Grade II** Neck pain, stiffness, tenderness. Clinical musculoskeletal signs including decreased range of motion and point tenderness.
- **Grade III** Neck pain, stiffness, tenderness. Clinical musculoskeletal signs include decreased range of motion and point tenderness. Neurological signs including decreased or absent deep tendon reflexes, weakness and sensory deficits.
- **Grade IV** Neck complaint and fractures or dislocations.

In addition to the above, related symptoms such as headache and tinnitus were included in the QTF classification scale [56].

To diagnose a patient with WAD, only Grade I, II, and III are used. Grade 0 will not lead to any diagnose and patients with Grade IV on the whiplash injury scale gets another diagnose. The QTF classification is the most commonly used [56], but other WAD classifications exist including *e.g.* psychological symptoms that are not part of the QTF scale [61–63]. The authors behind the QTF classification scale however highlighted a limitation in the lack of clinical objective findings to support clinical diagnosis of WAD [56].

Development of accurate imaging methods for muscle composition enables objective pathophysiological findings in the WAD cohort to explain the clinical findings. Potential findings could be differences in muscle composition comparing patients with WAD and healthy controls or detection of changes in muscle composition when developing chronic WAD.

Imaging and Patients with Chronic WAD

Most MRI studies on patients with WAD have measured cross-sectional area (CSA) at different cervical levels in the neck muscles [16, 64–69]. There is a large variation between the studies including conflicting results. One study (using ultrasonic images) reported smaller CSA in patients with WAD compared to healthy controls [64]. Other studies using MRI did not report any differences [65–67], while a third outcome was MRI-based studies reporting an increase in CSA for patients with chronic WAD compared to healthy controls

[16, 68, 69]. Furthermore, there is a large variety in the reported CSA of the multifidus muscles [16, 64–69]. The ambiguity could have several different causes. One reason for the variety in CSA could be due to different methodologies for slice selection and choice of muscle region. Using different oblique planes at slightly different locations could influence the CSA. Anatomical differences throughout the muscles would affect the precision of the measurement and a whole-volume approach might be beneficial. One aim of Paper II was to measure the CSA at four axial slices to determine potential differences between left and right side muscles and potential differences throughout the slices.

One explanation to the conflicting results regarding differences in CSA between patients with WAD and healthy controls could be different methodologies and different muscle definitions. Most CSA studies [64–67] have not investigated muscle composition but only the area under the outlined ROI.

When starting investigating MFI in WAD cohorts using MRI, Elliott *et al.* found greater fat infiltration in the neck extensor muscles in chronic WAD patients compared to healthy controls [16, 70]. The high MFI findings were more apparent in the deep extensor muscles, especially in the small multifidus muscles [16, 70] and were unique to those who developed chronic WAD [71]. Furthermore, the same group of investigators indicated that self-reported neck disability (using the neck disability index (NDI) [72]) after a whiplash injury is correlated with MFI in the deep neck extensor muscles [14]. The NDI is calculated based on a multi-choice self-reported form. NDI ranges from 0–100%, where 0% indicates no neck disability and 100% is maximum neck disability.

The findings had at the starting point of this thesis only been conducted on an American and an Australian cohort by a single group of investigators [16, 71]. Furthermore, those studies analyzed cross-sectional slices on T_1-weighted images. The studies had not yet utilized the advances of quantitative MFI using chemical shift imaging as *e.g.* proposed in Paper I and IV. Another aim of Paper II was therefore to investigate the potential differences in fat infiltration using high-resolution 2-point chemical shift encoded imaging on a new cohort.

The finding of greater fat infiltration in the multifidus muscles is intriguing, albeit the underlying causes are still unknown. One explanation of the higher fat infiltration in the multifidus muscles could be a local injury caused by the whiplash trauma, as proposed by Pedler *et al.* [73]. The multifidus muscles are directly inserted to the facet capsules of the cervical vertebrae, which makes it possible for the multifidus to be directly involved in a whiplash injury [74].

Several alternative explanations have been offered to explain the change in MFI in patients with WAD including heightened stress response [75–77], physical inactivity [78, 79], injury severity, pain intensity and/or related disability [14, 71], central/peripheral neuronal interference [80–82], and/or spinal cord injury [83].

Due to the large number of explanation models, more and extended studies are needed. One direction to potentially explain the mechanisms behind MFI in the multifidus muscles is to also investigate the widespread MFI in patients with WAD. Since some of the explanation models for increased MFI (as heightened stress response and physical inactivity) would likely not be isolated to multifidus but also appear for other muscles throughout the body. Two studies have investigated muscles distal to the cause of the whiplash trauma [73, 80]. However, the results were contradicting. One of the studies was a case study only including 4 participants while the other only investigated a single distal muscle. Furthermore, none of the studies involved a regression model to compare MFI local and distal to the site of the whiplash trauma.

Paper III therefore aimed to investigate widespread MFI and compare it to the MFI in whole-volume multifidus using a cohort similar in size to the one presented by Pedler *et al.* [73].

To summarize; in paper II, the CSA and MFI in the deep multifidus muscles were investigated bilaterally at cervical level C4–C7 as previously reported [16, 71], but using high resolution chemical shift encoded imaging at 3T. In paper III, the whole volume MFI in the multifidus was investigated and compared to widespread MFI (including all muscles below the hip joint) using the automatic method described in Chapter 2–4. Below follows a short summary of the method used and the findings. For a full description, see Paper II and Paper III.

Cohort

For this thesis, two studies were reported (Paper II and Paper III) in patients with chronic WAD (Grade II and Grade III according to the QTF classification [56]). Demographic data for the cohort used in Paper II and in Paper III are summarized in Table 1. The participants with chronic WAD were included from an on-going randomized controlled trial (RCT) comparing three different exercise strategies [84, 85]. Gender and age-matched (± 2 years) controls with no neck-related symptoms were also recruited. The included participants with chronic WAD were stratified into two groups based on the self-reported NDI scores. Mild/Moderate WAD included participants with an NDI score $< 40\%$ and severe WAD included participants with an NDI score $\geq 40\%$. The cut-off at 40% has previously been motivated for stratifying patients with WAD based on NDI [86].

Inclusion criteria for the WAD groups included: chronic disability of QTF Grade II or Grade III; more than 6 months and less than 3 years since injury; and pain intensity greater than 20 mm on a 100 mm visual analogue scale [87] alternatively a greater score than 20% on the NDI scale [72]. Exclusion criteria included generalized or more dominant pain elsewhere in the body; and other potentially confounding physical or psychological diseases. A full description

	Healthy Controls	Mild/Moderate WAD (NDI<40%)	Severe WAD (NDI ≥40%)
Participants (n)	31	20	11
Women (men) (n)	17(14)	10 (10)	7(4)
Age (y)	41.5±10.6 (22–61)	39.2±11.5 (20–62)	45.7±8.5 (34–58)
BMI (kg/m^2)	24.4±3.2 (19.7–34.5)	25.5±4.1 (19.1-33.8)	25.8±3.4 (20.3-32.3)
NDI (%)	n/a	27.3±6.8 (10–38)	51.3±10.2 (40–68)
Time since injury (mo)	n/a	20.1±9.8 (7–36)	14.5±7.2 (6–32)

Table 6.1: Demographic data for the cohorts used in Paper II and in Paper III. The rows *Participants* and *Women (men)* are in number of participants, n and *time since injury* is in months (mo). The remaining rows' values are mean ± SD (range).

of the inclusion/exclusion criteria for the WAD groups are reported in Paper II, Paper III, and by Peolsson *et al.* [85] and Ludvigsson *et al.* [84].

Inclusion/exclusion criteria for the healthy controls were gender and age matched (± 2 years) individuals with no present or past neck pain, dysfunction or related disability. Paper II and Paper III also include all exclusion criteria for the healthy controls. Data were acquired using parameter settings described in Table 2.1 in Chapter 2.

Image Segmentation

In Paper II, the CSA at cervical level C4, C5, C6 and C7 were outlined on both left and right side separately using AnalyzeDirect, described in Chapter 3. The different cervical levels are illustrated in Figure 6.1. Twenty of the images were outlined twice for investigating intra-reader reliability.

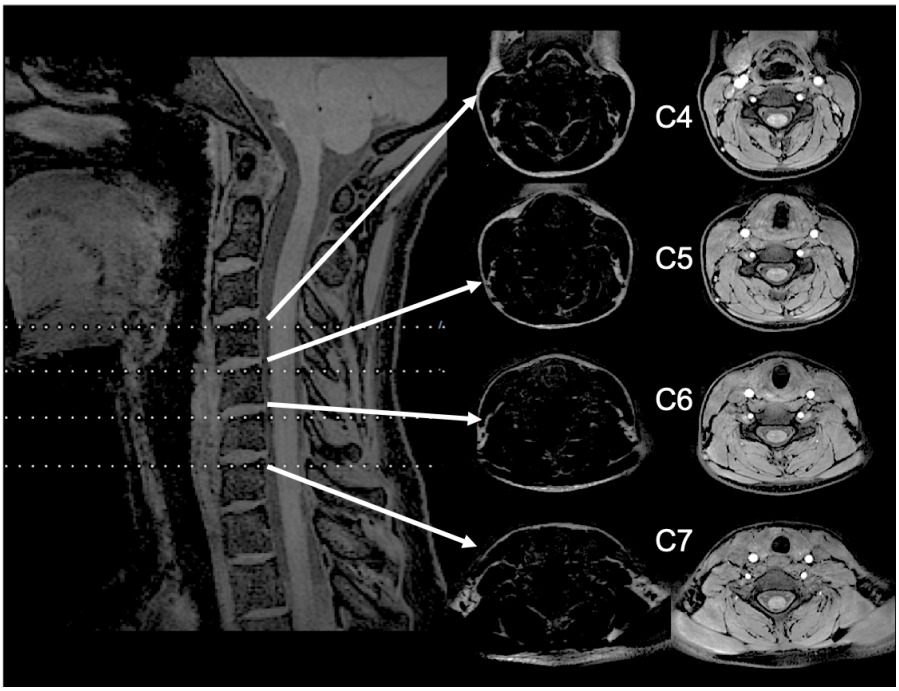

Figure 6.1: A sagittal slice (left) with marked axial slice selections for the cervical slices C4–C7. The axial images for fat (middle row) and water (right row) are shown at the right part of the image.

In Paper III, the whole-volume of multifidus on left and right side were outlined separately using the image foresting transform-based algorithm described in Chapter 3. The segmentation was cropped to only include data between the C4 and C7 axial levels. Twenty of the images were outlined twice for investigating intra-reader reliability.

In Paper III, the widespread MFI was calculated by the methods described in Chapters 2–4 where all muscles below the hip joint were included.

Statistics

In Paper II, a 3-way, 2-repeated-measures analysis of variance (ANOVA) was chosen as the model for investigating cross-sectional area and fat infiltration. The model included using the four segmental levels and the lateral sides as within-participant variability and group (healthy, mild/moderate WAD, severe WAD) as between participant variable. Separate ANOVAs were performed on CSA and MFI. Post-hoc tests with Bonferroni corrections for multiple comparisons were performed to investigate significant differences from the ANOVAs. A p-value < 0.05 was considered significant.

In Paper III three mixed linear models were used: (A) the association between MFI in multifidus with MFI in the lower extremities; (B) model A including group (healthy, mild/moderate WAD, severe WAD) and age as fixed factors; and (C) model B including BMI as a fixed factor. Furthermore, a linear regression analysis between MFI in multifidus and time since injury was made for the two WAD groups.

Segmentation Reliability

The intra-rater reliability was measured using a 2-way, random effects, single-measure ICC with absolute agreement.

The ICC for the eight cross-sectional areas (C4–C7 segmented bilaterally) ranged from 0.81–0.93 (95% confidence interval ranged from: 0.57–0.98). The ICC for MFI at the eight cross-sectional areas (C4–C7 segmented bilaterally) ranged from 0.82–0.97 (95% confidence interval ranged from: 0.60–0.99). The ICC for the MFI at the two whole-volumes (left and right side segmented separately) range from 0.90–0.95 (95% confidence interval ranged from: 0.76–0.98).

Cross-Sectional Area

No significant differences ($p = 0.41$) were found for CSA between the three different groups of participants, see Table 6.1 for group demographics. The CSA of the muscles were ranging from 238 mm^2 (C5) to 390 mm^2 (C7), which is approximately in the middle of reported CSAs in literature using MRI [16, 64–69].

However, significant differences ($p < 0.01$) in CSA were found for the different cervical levels, except between the CSA between level C4 and level C5 ($p = 0.13$). This highlights the sensitivity of slice selection when doing comparison and longitudinal studies.

Muscle Fat Infiltration

Significant differences were found for average CSA MFI between the different groups ($p = 0.025$ and $p = 0.018$ for separating severe WAD from healthy controls and mild/moderate WAD respectively). Significant differences were also found when the whole-volume was compared ($p < 0.001$ and $p < 0.005$ for separating severe WAD from healthy controls and mild/moderate WAD respectively). In Figure 6.2 the two different methods used for MFI in the multifidus are shown. Both methods showed consistent results of higher MFI between healthy controls and severe WAD as well as between mild/moderate WAD. No significant differences between mild/moderate and healthy controls were found.

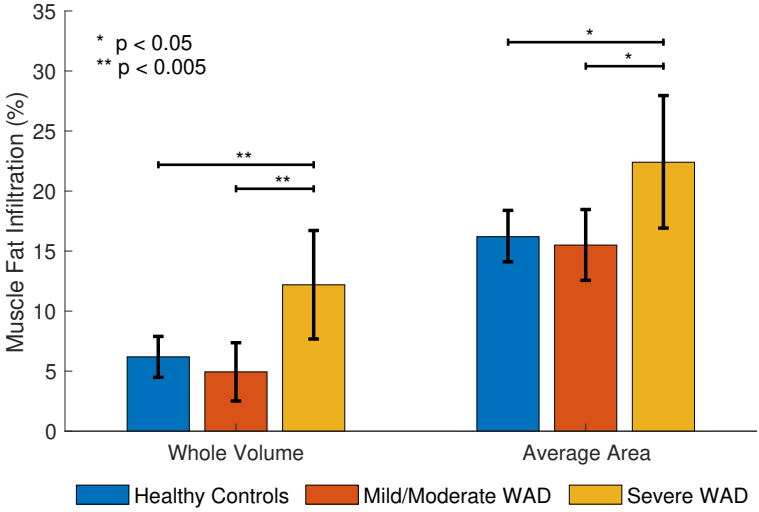

Figure 6.2: Comparing MFI between whole-volume ROI and average MFI of 4 cross-sectional slices of the multifidus muscles. The vertical whiskers are the 95% confidence level and the horizontal whiskers indicate significance between groups.

Paper III showed a significant correlation ($p < 0.001$) between MFI in multifidus and MFI in the lower extremities. The result remained significant when adjusting for age and group ($p = 0.009$) as well as when adjusting for BMI ($p = 0.002$).

Since the time since injury might be a confounding factor to the increased MFI in patients with severe WAD, a regression analysis was made. There was no significant ($p = 0.9$) association between MFI in multifidus and time since injury.

6.2 Other Clinical Studies

The method presented in this thesis has also been used in other studies beyond the scope of this thesis. A short summary of the studies is presented below to highlight the potential of the method besides patients with chronic WAD.

MFI and Rotator Cuff Muscles

In a study by Giambini *et al.* a positive correlation was found between fat-referenced MFI in the rotator cuff and muscle exensibility. No correlation was found when a high qualitatively determined fat content were analyzed against

muscle extensibility [88]. The authors argues that a non-invasive extensibility prediction, using *e.g.* quantitative fat fraction estimation may help in pre-surgical planning and post-operative evaluation of a rotator cuff tear.

Hypertrophy

In a study by Mandić *et al.* the automatic method was extended by including individual knee-extensor muscles. The method was both validated compared to manual quantification of knee-extensor muscles and to investigate potential detection of hypertrophy after a training program [89]. In the study, clinically relevant changes in muscle volume after the exercise intervention was found and the authors conclude that the automatic method is feasible for muscle analysis both in sports and for investigating clinical conditions [89].

Large-Cohort Studies

West *et al.* investigated the feasibility of a rapid neck-to-knee acquisition (6 minute scanning time) for analysis of muscle composition based on 3,000 data sets from the large UK Biobank cohort where a total of $100,000$ neck-to-knee data sets are acquired and will be analyzed using the methodology presented in this thesis [90].

Normative and Disease Profiling

The automated method presented in this thesis has also been used for determining age- and gender-dependent normative values for muscle volumes in a Swiss cohort [91]. The method was compared to anthropometric and to bio-electrical impedance measurements [91].

Another study used the method for associating coronary heart disease and type II diabetes to a multivariate body composition profiling [92]. The body composition profiling highlighted associations between multi-variable fat distributions in the body and different diseases. That study could not conclude association using solely a single fat compartment, why rapid large-coverage three-dimensional images are needed [92].

7

Discussion

In this thesis, a method for muscle composition analysis has been proposed, organized in four main steps: (1) data acquisition and reconstruction, (2) tissue segmentation, (3) feature extraction, and (4) data analysis. The proposed method is modular, meaning that each step can be optimized separately to best fit the need for specific clinical and/or research applications. Since the steps are linked, evaluation of a new combination might affect the final result. Several ways of combining the different steps were presented and evaluated. In this chapter, the main findings after developing a quantitative muscle composition analysis using chemical shift MRI are highlighted, in addition to the limitations being addressed and analyzed to propose potential future developments for the presented method.

7.1 Main Findings

In this section, the main findings of this thesis are addressed.

Whole-Volume Acquisition

One of the main strengths of this method is the possibility of whole-volume acquisition since one challenge of muscle composition analysis is the anatomical variance within the muscles, both in lean muscle volume and MFI. Therefore, results from cross-sectional slices could suffer from a high variability due to this anatomical variance. In Paper IV, a 40% increase in within-patient standard deviation (s_w) was observed for all muscles/muscle groups when only investigating the middle slice instead of whole-volume analysis. The benefit of whole-volume analysis was also indicated when comparing the results for fat infiltration measurements between the three different groups (Figure 6.2). The whole-volume analysis resulted in an increased significance of the difference between groups compared to the average CSA results. This might

be due to less relative influence of noise in the whole-body data acquisition. That is, the estimate will become less affected by signal noise upon adding voxels. Another benefit of whole-volume acquisition is that it is not dependent on a consistent placement of cross-sectional slices, which is a problem in 2D acquisition.

A single axial slice is difficult to reproduce. In Paper IV, the middle slice was acquired based on the automatic segmentation, which took other anatomical landmarks into account for slice selection. However, defining good landmarks might be difficult for some muscles, and the muscle is not necessarily in the same position and at the same angle. Due to the anatomical variation of the MFI throughout the muscles [93, 94], whole-volume muscle analysis is superior.

Robustness and Versatility of the Method

The automatically acquired muscle volume showed a high accuracy, which was manifested in two ways. First, the proposed whole-body volume analysis showed a high accuracy compared to the manual reference method. Second, the proposed method was reproducible *i.e.* reported similar muscle volumes, both for regional and whole-body volumes, despite the change in field strength, different flip angles, and the 8-fold resolution difference. The reported results are in line with other methods in literature [19].

Furthermore, the method showed high robustness, both for muscle volume acquisition and fat infiltration. For muscle volume, the method showed similar delta-volumes and as high ICC as the manual reference method when applied to a new validation data set not used for optimization. Also, the fat infiltration shows an insensitivity to choice of flip angle as the fat-referenced estimate did not change when using different flip angles, which was the case for fat-fraction calculations.

The body composition analysis showed high reproducibility both for fat infiltration and muscle volume. The MFI also showed a robustness to slight changes in acquisition parameters as the precision does not change when varying the flip angle between 5° and 10°. This is a great benefit since the *true* acquisition flip angle might be different from the *desired* flip angle due to *e.g.* eddy currents and B_1-inhomogeneites. In this thesis, the reproducibility between two different scanners at two different field strengths was tested. According to a review article investigating automatic fat and muscle composition methods reported between 2013 and 2018, Paper I was the only one reporting muscle volume reproducibilty [49].

Another finding of the presented automatic atlas-based algorithm was that neither age nor BMI affected the performance of the algorithm. The individuals in the validation data set had a much higher mean age than the individuals in the atlas data set but it resulted in high ICC values and low delta-volumes compared to the manual reference. Even though 8 of the 10 individuals in

the atlas data set were lean (i.e. a BMI between 18–25), they could be used as atlases with good results on the validation set where the participants were slightly heavier. The robustness of the multi-atlas segmentation against varying BMI was also confirmed in the study by Thomas *et al.* [55] where the same atlases (n = 11) were registered onto 10 lean, 10 overweight (BMI = 25–30) and 10 obese (BMI > 30) participants [55].

One advantage of the multi-atlas registration technique is the effective way of adding more features to the atlas database. If more muscle definitions are to be added, it is easily done. The multi-atlas database needs only a few subjects to be useful and they can be chosen wisely depending on the targets of interest. Furthermore, the supervised automated muscle segmentation, used in Paper IV, gives the possibility to correct the segmentation if needed, which is not straight-forward with many other automatic segmentation methods.

The quantitative assessment of muscle volume and fat infiltration is a requirement for longitudinal studies in order to be used as potential biomarkers with cut-off values. Although more studies should be conducted with other scanner parameters to evaluate the full potential of the method, Paper I and Paper IV do suggest promising quantitative estimates for muscle volume and MFI that are both accurate and precise.

Removal of Larger Fatty Streaks

In Paper I, the accuracy improved using the fat-free muscle mask M_{FF} or the lean muscle mask M_{L} compared to the whole muscle mask M_{M}. One reason is that the effect of leakage to surrounding subcutaneous tissue due to errors in the segmentation algorithm is minimized. Contributions from larger inter-muscle fat are also removed.

When comparing the two different methods for acquiring MFI in the multifidus (cross-sectional slices and whole-volume) it was found that whole-volume analysis leads to a better repeatability, as mentioned above. Another finding was the difference in the mean MFI between the two methodologies. In the two papers, the same cohort was used (using the same images from the same acquisition in the analysis). The difference in the results stems from the definition of the ROI. Although it was two different investigators, the type of segmentation method is likely to be the main reason that the cross-sectional method reported higher mean MFI throughout the three different groups. The contour-based method used the fat images and included all voxels within the contour. The volume-based method instead used the water images, which might have excluded voxels with high fat content from the ROI. Investigations with removal of larger fat streaks using Equation 4.7 could result in a more similar fat estimate when comparing the two methodologies. However, this was not evaluated in this thesis due to an unsuccessful calibration to fat-referenced images; see Section 7.2.

Since there is a large ambiguity in findings on patients with chronic WAD, there is need for accurate and reproducible tools in order to perform quantitative longitudinal and multi-center studies. A standardized methodology for analyzing the neck muscles has also been proposed [95, 96]. The proposed technique suggests a flip angle of 5° for data acquisition [95], which will most likely result in T_1-bias if not using a technique where the fat is calibrated with itself as reference, *e.g.* the fat-referenced technique presented here. Evaluation of the accuracy and repeatability of the standardized methodology are also needed.

7.2 Limitations

Due to scanner limitations such as limited FOV and field inhomogeneities further out in the FOV, the arms provide challenges against acquiring precise results in fully automated whole-body MR acquisitions. For investigation of general muscle composition, arms should therefore be excluded from the analysis. Since the thigh muscles contain >40% of the total amount of muscle volume (see Table 1 in Paper I) they can provide a representation of the general muscle composition analysis. In the legs, excellent automated results was shown, which would give a precise and repeatable estimate of the general muscle composition without being affected by high variability due to arm placement. However, when the arms are of interest, a separate acquisition apart from the whole-body scan should be considered for non-lean individuals.

This thesis evaluated the whole-body and regional muscle compartments on healthy volunteers with no known muscle dystrophy. Likely, the atlas database would benefit from adding patients with a variety of muscle compositions followed by a smart selection of prototypes prior to image registration. In Paper I, an automated selection of prototypes was performed by an iterative process where a full set of atlases was used in the first iteration. In the second iteration, the atlases with most similar muscle composition were used in the probability-voting. While this solution might help when the muscle composition across patient cohorts looks different, it has not been investigated in this thesis.

Another limitation in this thesis was the inability to calibrate the high-resolution images to fat-referenced images. The neck muscles were acquired using longer echo-times to provide the high resolution ($0.75 \times 0.75 \times 0.75$ mm^3) images. The implementation of the fat-referenced CIIC algorithm was challenging as a result of the combination of inhomogeneities, acquired image resolution, and the different relationships between the fat and water signals due to the later echoes. The algorithm was at the time not tuned to handle the different parameter settings for acquiring the data for Paper II and Paper III. In situations where fat-referenced calibration is not possible, fat fraction is an alternative [24], which was used in Paper II and Paper III. However, since

the data was acquired using a 10° flip angle it is likely that an overestimation of the MFI has occurred due to T_1-bias. In Paper IV the fat fraction estimate was shown to provide similar repeatability to fat-referenced MFI. Therefore, conclusions about differences between WAD groups are still considered to be valid even when considering the potential bias in the estimate.

7.3 Future Work

While the muscle composition analysis method presented here has high potential and is already used today for large research studies [90, 92], the method also has room for improvement, to be refined and even more versatile.

First, as discussed in Section 7.2, the high-resolution images were not calibrated with CIIC into fat-referenced images. Instead quantification was made using fat fraction, yielding a potential T_1-bias in the MFI estimate. At the time of writing this thesis, data for a new study investigating participants with WAD are acquired, described by the study protocol by Peolsson *et al.* [97]. In that study, a slightly lower image resolution is used to utilize the benefit of fat-referenced images without T_1-bias while keeping a good SNR with a higher flip angle. The new acquired resolution should still be sufficient as it is in line with the proposed resolution presented by Crawford *et al.* [95].

In Paper III, an association between fat in the lower extremities (far from the site of the whiplash injury) and the more closely located multifidus muscles was found. However, the difference in lower extremities' MFI among the three groups was not significant. This might imply that the whiplash movement injures the muscles locally, or simply that the study cohort was not large enough. Further investigations on whole-body data in the whiplash cohort are needed to draw any conclusions, especially since literature provides contradicting results [73, 80]. Due to the automated segmentation of thigh muscles, the proposed method could be applied effectively in research studies. The ability to extend the automated method to also include the neck-specific images would make the analysis of multifidus more efficient. Automated neck muscle segmentation has recently been proposed in literature, *e.g.* by using neural networks [98]. Automation of neck segmentation was not part of the scope of this thesis but nothing specifically hinders the automated technique proposed in this thesis to be applied also to neck images.

Extended method evaluations on different scanner manufacturers and varying scanner parameters could further test the versatility of the proposed method. For instance, testing repeatability and noise characteristics using several different flip angles in the range from *e.g.* 1 to 20 would be very valuable to fully investigate the potential in-sensitivity to flip angle with the fat-referenced technique.

Lastly, to further evaluate the feasibility of the method on other clinical cohorts *e.g.* pre-surgical planning of rotator cuff tears or normative and disease profiling in large-cohorts studies would be valuable, see also Section 6.2.

7.4 Conclusions

One of the biggest challenges of this thesis has also been the greatest potential advantage. The challenge is that this thesis work includes protocol optimization, image post-processing, image analysis, and data analysis. Each of the different links/steps affects the end result and each can be optimized separately. However, for a method to be useful, good knowledge of a single step is not enough. In order to combine a good set of links for the data analysis and construct the optimal muscle composition analysis method, each step must be optimized considering all other steps. The *optimal* method might also be different for different clinical needs or different clinical settings.

In this thesis, I aimed to present such a method that automatically and rapidly could extract accurate and precise quantitative volumes and fat infiltration for individual muscles, muscle groups and whole-body data. Another objective was to propose a method for high-resolution image acquisition for whole-volume data analysis on the small multifidus muscles after a whiplash injury. The proposed method shows a high versatility including successful usage in a clinical cohort. By combining the steps/links carefully, the aims have been fulfilled.

Bibliography

1. Foley, S., Ding, C., Cicuttini, F. & Jones, C. Physical Activity and Knee Structural Change: A Longitudinal Study Using MRI. *Medicine & Science in Sports & Exercise.* https://doi.org/10.1007/s002560000238 (2000).

2. Emery, E. H. The muscular dystrophies. *The Lancet.* https://doi.org/10.1016/S0140-6736(02)07815-7 (2002).

3. Willis, T. A., Hollingsworth, K. G., Coombs, A., Sveen, M.-L., Andersen, S., Stojkovic, T., Eagle, M., Mayhew, A., de Sousa, P. L., Dewar, L., Morrow, J. M., Sinclair, C. D. J., Thornton, J. S., Bushby, K., Lochmüller, H., Hanna, M. G., Hogrel, J.-Y., Carlier, P. G., Vissing, J. & Straub, V. Quantitative Muscle MRI as an Assessment Tool for Monitoring Disease Progression in LGMD2I: A Multicentre Longitudinal Study. *PLoS ONE.* https://doi.org/10.1371/journal.pone.0070993 (2013).

4. Bonati, U., Hafnerb, P., Schädelinc, S., Schmida, M., Devasiaa, A. N., Schroedera, J., Zueslia, S., Pohlmana, U., Neuhausd, C., Kleine, A., Sinnreichb, M., Haasg, T., Gloorg, M., Bierig, O., Fischmannh, A. & Fischer, D. Quantitative muscle MRI: A powerful surrogate outcome measure in Duchenne muscular dystrophy. *Neuromuscular Disorders.* https://doi.org/10.1016/j.nmd.2015.05.006 (2015).

5. Willcocks, R. J., Rooney, W. D., Triplett, W. T., Forbes, S. C., Lott, D. J., Senesac, C. R., Daniels, M. J., Wang, D., Harrington, A. T., Tennekoon, G. I., Russman, B. S., Finanger, E. L., Byrne, B. J., Finkel, R. S., Walter, G. A., Sweeney, H. L. & Vandenborne, K. Multicenter prospective longitudinal study of magnetic resonance biomarkers in a large duchenne muscular dystrophy cohort. *Annals of Neurology.* https://doi.org/10.1002/ana.24599 (2016).

6. Garcia, J. MRI in inflammatory myopathies. *Skeletal Radiology.* https://doi.org/10.1249/mss.0b013e31802d97c6 (2007).

7. Cruz-Jentoft, A. J., Baeyens, J. P., Bauer, J. M., Boirie, Y., Cederholm, T., Landi, F., Martin, F. C., Michel, J.-P., Rolland, Y., Schneider, S. M., Topinková, E., Vandewoude, M. & Zamboni, M. Sarcopenia: European consensus on definition and diagnosis: Report of the European Working Group on Sarcopenia in Older People. *Age and Ageing.* https://doi.org/10.1093/ageing/afq034 (2010).

8. Cruz-Jentoft, A. & (eds.), J. M. *Sarcopenia* (Somerset, NJ: Wiley-Blackwell, 2012).

9. A.Fielding, R., BrunoVellas, J.Evans, W., Bhasin, S., E.Morley, J., B.Newman, A., van Kan, G. A., Andrieu, S., Bauer, J., Breuille, D., Cederholm, T., Chandler, J., Meynard, C. D., Donini, L., Harris, T., Kannt, A., Guibert, F. K., Onder, G., Papanicolaou, D., Rolland, Y., Rooks, D., Sieber, C., Souhami, E., Verlaan, S. & Zamboni, M. Sarcopenia: An Undiagnosed Condition in Older Adults. Current Consensus Definition: Prevalence, Etiology, and Consequences. International Working Group on Sarcopenia. *Journal of the American Medical Directors Association.* https://doi.org/10.1016/j.jamda.2011.01.003 (2000).

10. Zoico, E., Rossi, A., Francesco, V. D., Sepe, A., Olioso, D., Pizzini, F., Fantin, F., Bosello, O., Cominacini, L., Harris, T. B. & Zamboni, M. Adipose Tissue Infiltration in Skeletal Muscle of Healthy Elderly Men: Relationships With Body Composition, Insulin Resistance, and Inflammation at the Systemic and Tissue Level. *J Gerontol A Biol Sci Med Sci.* https://doi.org/10.1093/gerona/glp155 (2010).

11. Delmonico, M. J., Harris, T. B., Visser, M., Park, S. W., Conroy, M. B., Velasquez-Mieyer, P., Boudreau, R., Manini, T. M., Nevitt, M., Newman, A. B. & Goodpaster, B. H. Longitudinal study of muscle strength, quality, and adipose tissue infiltration. *Am J Clin Nutr.* https://doi.org/10.3945/ajcn.2009.28047 (2010).

12. Goodpaster, B. H., Stenger, V. A., Boada, F., McKolanis, T., Davis, D., Ross, R. & Kelley, D. E. Skeletal muscle lipid concentration quantified by magnetic resonance imaging. *The American Journal of Clinical Nutrition.* https://doi.org/10.1093/ajcn/79.5.748 (2004).

13. Gerdle, B., Forsgren, M. F., Bengtsson, A., Dahlqvist Leinhard, O., Sören, B., Karlsson, A., Brandejsky, V., Lund, E. & Lundberg, P. Decreased muscle concentrations of ATP and PCR in the quadriceps muscle of fibromyalgia patients - A ^{31}P-MRS study. *European Journal of Pain* (2013).

14. Elliott, J., Pedler, A., Kenardy, J., Galloway, G., Jull, G. & Sterling, M. The temporal development of fatty infiltrates in the neck muscles following whiplash injury: an association with pain and posttraumatic stress. *PLoS one.* 10.1371/journal.pone.0021194 (2011).

15. Carroll, L. J., Holm, L. W., Hogg-Johnson, S., Côté, P., Cassidy, J. D., Haldeman, S., Nordin, M., Hurwitz, E. L., Carragee, E. J., van der Velde, G., Peloso, P. M. & Guzman, J. Course and Prognostic Factors for Neck Pain in Whiplash-Associated Disorders (WAD): Results of the Bone and Joint Decade 2000-2010 Task Force on Neck Pain and Its Associated Disorders. *Spine* (2008).

16. Elliott, J. M., Jull, G., Noteboom, J., R, R. D., Galloway, G. & Gibbon, W. Fatty infiltration in the cervical extensor muscles in persistent whiplash-associated disorders: a magnetic resonance imaging analysis. *Spine* (2006).

17. Elliott, J. M., Kerry, R., Flynn, T. & Parrish, T. Content not quantity is a better measure of muscle degeneration in whiplash. *Manual Theraphy,* 1–5 (2013).

18. Joyce, N. C., Oskarsson, B. & Jin, L.-W. Muscle Biopsy Evaluation in Neuromuscular Disorders. *Phys Med Rehabil Clin N Am.* https://doi.org/10.1016/j.pmr.2012.06.006 (2012).

19. Broderick, B. J., Dessus, S., A.Grace, P. & Ó'Laighin, G. Technique for the computation of lower leg muscle bulk from magnetic resonance images. *Medical Engineering & Physics.* https://doi.org/10.1016/j.medengphy.2010.06.008 (2010).

20. Brunner, G., Nambi, V., Yang, E., Kumar, A., Virani, S. S., Kougias, P., Shah, D., Lumsden, A., Ballantyne, C. M. & D.Morrisett, J. Automatic quantification of muscle volumes in magnetic resonance imaging scans of the lower extremities. *Magnetic Resonance Imaging.* https://doi.org/10.1016/j.mri.2011.02.033 (2011).

21. Wald, D., Teucher, B., Dinkel, J., Kaaks, R., Delorme, S., Meinzer, H.-P. & Heimann, T. *Automated quantification of adipose and skeletal muscle tissue in whole-body MRI data for epidemiological studies* in *In Proceedings of SPIE Medical Imaging* (2012).

22. Baudin, P. Y., Azzabou, N., Carlier, P. G. & Paragios, N. Prior knowledge, random walks and human skeletal muscle segmentation. *Med Image Comput Comput Assist Interv.* https://doi.org/10.1007/978-3-642-33415-3_70 (2012).

23. Hu, H. H., Branca, R. T., Hernando, D., Karampinos, D. C., Machann, J., McKenzie, C. A., Wu, H. H., Yokoo, T. & Velan, S. S. Magnetic resonance imaging of obesity and metabolic disorders: Summary from the 2019 ISMRM workshop. *Magnetic Resonance in Imaging* (2019).

24. Romu, T. *Fat-Referenced MRI* PhD thesis (Linköping University, 2018).

25. Berglund, J. *Separation of Water and Fat Signal in Magnetic Resonance Imaging: Advances in Methods Based on Chemical Shift* PhD thesis (Uppsala University, 2011).

26. Ren, J., Dimitrov, I., Sherry, A. D. & Malloy, C. R. Composition of adipose tissue and marrow fat in humans by 1H NMR at 7 Tesla. *Journal of lipid research.* 49.9, pp. 2055-2062 (2008).

27. Gold, G. E., Han, E., Stainsby, J., Wright, G., Brittain, J. & Beaulieu, C. Musculoskeletal MRI at 3.0 T: Relaxation Times and Image Contrast. *The American Journal of Roentgenology.* https://doi.org/10.2214/ajr.183.2.1830343 (2004).

28. Denolin, V., Azizieh, C. & Metens, T. New insights into the mechanisms of signal formation in RF-spoiled gradient echo sequences. *Magnetic Resoance in medicine* (2005).

29. Hernando, D., Liang, Z.-P. & Kellman, P. Chemical shift-based water/fat separation: a comparison of signal models. *Magnetic Resonance in Imaging.* pp. 811-822 (2010).

30. Dixon, W. T. Simple Proton Spectroscopic Imaging. *Radiology* (1984).

31. Berglund, J., Ahlström, H., Johansson, L. & Kullberg, J. Two-point dixon method with flexible echo times. *Magnetic Resonance in Medicine.* https://doi.org/10.1002/mrm.22679 (2011).

32. Berglund, J. & Kullberg, J. Three-dimensional water/fat separation and T_2^* estimation based on whole-image optimization—Application in breathhold liver imaging at 1.5 T. *Magnetic Resonance in Medicine.* https://doi.org/10.1002/mrm.23185 (2012).

33. Hernando, D., Haldar, J. P., Sutton, B. P., Ma, J., Kellman, P. & Liang, Z. Joint estimation of water/fat images and field inhomogeneity map. *Magnetic Resonance in Imaging.* https://doi.org/10.1002/mrm.21522 (2008).

34. Ma, J. Dixon techniques for water and fat imaging. *Journal of Magnetic Resonance Imaging.* https://doi.org/10.1002/jmri.21492 (2008).

35. Reeder, S. B., Pineda, A. R., Wen, Z., Shimakawa, A., Yu, H., Brittain, J. H., Gold, G. E., Beaulieu, C. H. & Pelc, N. J. Iterative decomposition of water and fat with echo asymmetry and least-squares estimation (IDEAL): Application with fast spin-echo imaging. *Magnetic Resonance in Medicine.* https://doi.org/10.1002/mrm.20624 (2005).

36. Yu, H., McKenzie, C. A., Shimakawa, A., Vu, A. T., Brau, A. C., Beatty, P. J., Pineda, A. R., Brittain, J. H. & Reeder, S. B. Multiecho reconstruction for simultaneous water-fat decomposition and T2* estimation. *Journal of Magnetic Resonance Imaging.* https://doi.org/10.1002/jmri.21090 (2007).

37. Rydell, J., Knutsson, H., Pettersson, J., Johansson, A., Farnebäck, G., Dahlqvist, O., Lundberg, P., Nyström, F. & Borga, M. *Phase sensitive reconstruction for water/fat weparation in MR imaging using iverse gradient* in *In: Medical Image Computing and Computer-Assisted Intervention-MICCAI 2007* (2007).

38. Romu, T., Dahlström, N., Leinhard, O. D. & Borga, M. Robust water fat separated dual-echo MRI by phase-sensitive reconstruction. *Magnetic Resonance in Medicine.* pp. 1208-1216 (2017).

39. Song, S. M.-H., Napel, S., Pelc, N. J. & Glover, G. H. Phase unwrapping of MR phase images using Poisson equation. *In: IEEE Transactions on Image Processing.* 667-676 (1995).

40. Reeder, S. B., Hu, H. H. & Sirlin, C. B. Proton deinsity fat-fraction: A standardized mr-based biomarker of tissue fat concentration. *Magnetic Resonance in Medicine.* 36.5, pp. 1011-1014 (2012).

41. Liu, C.-Y., McKenzie, C. A., Yu, H., Brittain, J. H., Reeder, J. H. & Reeder, S. B. Fat quantification with IDEAL gradient echo imaging: correction of bias from T1 and noise. *Magnetic Resonance Imaging.* 58(2):354-364 (2007).

42. Hu, H. & Nayak, K. S. Quantification of absolute fat mass using an adipose tissue reference signal model. *Journal of Magnetic Resonance Imaging.* pp.1483-1491 (2008).

43. Dahlqvist Leinhard, O., Johansson, A., Rydell, J., Smedby, Ö., Nyström, F., Lundberg, P. & Borga, M. *Quantitative abdominal fat estimation using MRI* in *In: Proceeding International Conference on Pattern Recognition (ICPR)* (2008).

44. Romu, T., Borga, M. & Dahlqvist Leinhard, O. *MANA- Multi scale Adaptive Normalized Averaging* in *In: Proceeding of International Symposium on Biomedical Imaging (ISBI)* (2011).

45. Andersson, T., Romu, T., Karlsson, A., Norén, B., Forsgren, M. F., Smedby, Ö., Kechagias, S., Almer, S., Lundberg, P., Borga, M. & Leinhard, O. D. Consistent intensity inhomogeneity correction in water-fat MFI. *Journal of Magnetic Resonance Imaging.* `https://doi.org/10.1259/bjr.20180252` (2015).

46. Hu, H. H., Li, Y., Nagy, T. R., Goran, M. I. & Nayak, K. S. Quantification of Absolute Fat Mass by Magnetic Resonance Imaging: a Validation Study against Chemical Analysis. *Int J Body Compos Res* (2011).

47. Peterson, P., Romu, T., Brorson, H., Leinhard, O. D. & Månsson, S. Fat quantification in skeletal muscle using multigradient-echo imaging: Comparison of fat and water references. *Journal of Magnetic Resonance Imaging.* 14:311. `https://doi.org/10.1002/jmri.24972` (2016).

48. Malmberg, F., Lindblad, J. & Nyström, I. *Sub-pixel segmentation with the image foresting transform* in *In Proceedings of the 13th International Workshop on Combinatorial Image Analysis (IWCIA)* (2009), 201–211.

49. Borga, M. MRI adipose tissue and muscle composition analysis - a rewiew of automation techniques. *Br J Radiol.* `https://doi.org/10.1259/bjr.20180252` (2018).

50. Knutsson, H. & Andersson, M. *Morphons: segmentations using elastic cancas and paint on priors* in *In Proceedings from IEEE International Conference on Image Processing (ICIP2005), Genova. Italy* (2005).

51. Hu, H., Chen, J. & Shen, W. Segmentation and quantification of adipose tissue by magnetic resonance imaging. *MAGMA* (2016).

52. Peng, Q., McColl, R. W., Ding, Y., Wang, J., Chia, J. M. & Weatherall, P. T. Automated method for accurate abdominal fat quantification on water-saturated magnetic resonance images. *Journal of Magnetic Resonance in Imaging.* `https://doi.org/10.1002/jmri.21040` (2007).

53. West, J., Romu, T., Thorell, S., Lindblom, H., Berin, E., Holm, A.-C. S., Åstrand, L. L., Karlsson, A., Borga, M., Hammar, M. & Leinhard, O. D. Precision of MRI-based body composition measurements of postmenopausal women. *PLoS ONE* (2018).

54. Dice, L. R. Measures of the Amount of Ecologic Association Between Species. *Ecology.* `https://doi.org/10.2307/1932409` (1945).

55. Thomas, M. S., Newman, D., Dahlqvist Leinhard, O., Kasmai, B., Greenwood, R., Malcolm, P. N., Karlsson, A., Rosander, J., Borga, M. & Toms, A. P. Test-retest reliability of automated whole body and compartmental muscle volume measurement on a wide bore 3T MR system. *European Radiology.* 4(10):739-47 (2014).

56. Spitzer, W., Skovron, M., Salmi, L., Cassidy, J., Duranceau, J., Suissa, S. & Zeiss, E. Scientific monograph of the Quebec Task Force on Whiplash Associated Disorders: redefining "whiplash" and its management. *Spine.* PMID: 7604354 (1995).

57. Holm, L., Carroll, L., Hogg-Johnsson, S., Cote, P., Guzman, J. & et.al. The burden and determinatnts of neck pain in whiplash-associated disorders after traffic collisions: results of the Bone and Joint Decade 2000-2010 Task Force on Neck Pain and Its Associated Disorders. *Spine.* 33(4 Suppl):S52-9 (2008).

58. Styrke, J., Stalnacke, B., Bylund, P., Sojka, P. & Bjornstig, U. A 10-year incidence of acute whiplash injuries after road traffic crashes in a defined ppulation in northern Sweden. *Pm R.* 4(10):739-47 (2012).

59. Leth-Petersen, S. & Rotger, G. Long-term labour-marked performance of whiplash claimants. *Journal of health economics.* 31(4):294-303. `https://doi.org/10.1016/j.healeco.2009.06.013` (2009).

60. Rebbeck, T., Sindhusake, D., Cameron, I., Rubin, G., Feyer, A. & et.al, J. W. A prospective cohort study of health outcomes following whiplash associated disorders in an Australian population. *Injury prevention: journal of the International Society for Child and Adolescent Injury Prevention.* 12(2):93-8 (2006).

61. Poorbaugh, K., Brismee, J., Phelps, V. & jr Sizer, P. S. Late whiplash syndrome: a clinical science approach to evidence-based diagnosis and management. *Pain Practice.* 8(1):65-67 (2008).

62. Soderlund, A. & Denison, E. Classification of patients with whoplash associated disorders (WAD): reliable and valid subgroups based on the Multidimensional Pain Inventory (MPI-S). *European Journal of Pain.* 10(2):113-9 (2006).

63. Sterling, M. A proposed new classification system for whiplash associated disorders - implications for assessment and management. *Manual Therapy.* 9(2):60-70 (2004).

64. Kristjansson, E. Reliability of ultrasonography for the cervical multifidus muscle in asymptomatic and symptomatic subjects. *Manual Theraphy.* 9(2),p.83-88 (2004).

65. Ulbrich, E., Anderson, S., Busato, A., Abderhalden, S., Boesch, C., Zimmermann, H., Heini, P., Hodler, J. & Sturzenegger, M. Cervical muscle area measurementes in acute whiplash patients and controls. *Journal of Magnetic Resonance Imaging.* `https://doi.org/10.1002/jmri.22446` (2011).

66. Ulbrich, E., Aeberhard, R., Wetli, S., Busato, A., Boesh, C., Zimmermann, H., Hodler, J., Anderson, S. & Sturzenegger, M. Cervical muscle area measurements in whiplash patients: Acute, 3, and 6 months folow-up. *Journal of Magnetic Resonance in Medicine.* 4(10):739-47. `https://doi.org/10.1002/jmri.23769` (2012).

67. Matsumoto, M., Ichihara, D., Okada, E., Chiba, K., Toyama, Y., Fuijwara, H., Momoshima, S., Nishiwaki, Y. & Takahata, T. Cross-sectional area of the posterior extensor muscles of the cervical spine in whiplash injury patients versus healthy volunteers – 10 year follow-up MR study. *Injury.* `https://doi.org/10.1016/j.injury.2012.01.017` (2012).

68. Elliott, J., Jull, G., Noteboom, J. & Galloway, G. MRI study of the cross-sectional area for the cervical extensor musculature in patients with persistent whiplash associated disorders (WAD). *Manual Therapy* (2008).

69. Elliott, J., Sterling, M., Noteboom, J., Darnell, D., Galloway, G. & Jull, G. Fatty infiltrate in the cervical extensor muscles is not a feature of chronic, insidious-onset neck pain. *Clinical Radiology* (2008).

70. Elliott, J. M., O'Leary, S., Sterling, M., Hendrikz, J., Pedler, A. & Jull, G. Magnetic resonance imaging findings of fatty infiltrate in the cervical flexors in chronic whiplash. *Spine* (2010).

71. Elliott, J. M., Courtney, D. M., Radermaker, A., Pinto, D., Sterling, M. & Parrish, T. B. The Rapid and Progressive Degeneration of the Cervical Multifidus in Whiplash: An MRI Study on Fatty Infiltration. *Spine.* 10.1097/BRS.0000000000000891 (2011).

72. Vernon, H. & Mior, S. The Neck Disability Index: a study of reliablity and validity. *Journal of manipulative and physiological therapeutics.* PMID: 1834753, 4(10):739–47 (1991).

73. Pedler, A., McMahon, K., Galloway, G., Durbridge, G. & Sterling, M. Intramuscular fat is present in cervical multifidus but not soleus in patients with chronic whiplash associated disorders. *PLoS ONE.* https://doi.org/10.1371/journal.pone.0197438 (2018).

74. Anderson, J. S., Hsu, A. W. & Vasavada, A. N. Morphology, architecture, and biomechanics of human cervical multifidus. *Spine* (2005).

75. Linnstaedt, S. D., Walker, M. G., Parker, J. S., Yeh, E., Sons, R. L., Zimny, E., Lewandowski, C., Hendry, P. L., Damiron, K., Pearson, C., Velilla, M.-A., O'Neil, B. J., Jones, J., Swor, R., Domeier, R., Hammond, S. & McLean, S. A. MicroRNA circulating in the early aftermath of motor vehicle collision predict persistent pain development and suggest a role for microRNA in sex-specific pain differences. *Mol Pain.* 11:66. https://doi.org/10.1186/s12990-015-0069-3 (2015).

76. Linnstaedt, S. D., Riker, K. D., Walker, M. G., Nyland, J. E., Zimny, E., Lewandowski, C., Hendry, P. L., Damiron, K., Pearson, C., Velilla, M.-A., Jones, J., Swor, R. A., Domeier, R. & McLean, S. A. MicroRNA 320a Predicts Chronic Axial and Widespread Pain Development Following Motor Vehicle Collision in a Stress-Dependent Manner. *The Journal of orthopaedic and sports physical therapy.* 46(10):911-919. https://doi.org/10.2519/jospt.2016.6944 (2016).

77. McLean, S. A. The potential contribution of stress systems to the transition to chronic whiplash-associated disorders. *Spine.* https://doi.org/10.1097/BRS.0b013e3182387fb4 (2011).

78. Manini, T. M., Clark, B. C., Nalls, M. A., Goodpaster, B. H., Ploutz-Snyder, L. L. & Harris, T. B. Reduced physical activity increases intermuscular adipose tissue in healthy young adults. *The American Journal of Clinical Nutrition.* https://doi.org/10.1093/ajcn/85.2.377 (2007).

79. Clark, B. C. In vivo alterations in skeletal muscle form an function after disuse atrophy. *Medicine and science in sports and exercise.* 10.1249/MSS.0b013e3181a645a6 (2009).

80. Elliott, J. M., Dewal, J. P. A., Hornby, T. G., Walton, D. M. & Parrish, T. B. Mechanisms Underlying Chronic Whiplash: Contributions from an Incomplete Spinal Cord Injury? *Pain Medicine.* https://doi.org/10.1111/pme.12518 (2014).

81. Guéz, M., Hildingsson, C., Rosengren, L., Karlsson, K. & Toolanen, G. Nervous Tissue Damage Markers in Cerebrospinal Fluid after Cervical Spine Injuries and Whiplash Trauma. *Journal of Neurotrauma.* https://doi.org/10.1089/089771503322385782 (2004).

82. Smith, A. C., Parrish, T. B., Hoggarth, M. A., McPherson, J. G., Tysseling, V. M., Wasielewski, M., Kim, H. E., Hornby, T. G. & Elliott, J. M. Potential associations between chronic whiplash and incomplete spinal cord injury. *Spinal Cord Ser Cases.* https://doi.org/10.1038/scsandc.2015.24 (2015).

83. Elliott, J. M., Pedler, A. R., Cowin, G., Sterling, M. & McMahon, K. Spinal cord metabolism and muscle water diffusion in whiplash. *Spinal Cord.* https://doi.org/10.1038/sc.2011.17 (2012).

84. Ludvigsson, M., Peterson, G., O'Leary, S., Dedering, A. & Peolsson, A. The Efect of Neck-specific Exercise with, or without a behavioral approach,on pain, disability and self-efficacy in chronic whiplash-assosciated disorders: a radomized clinical trial. *The clinical journal of pain.* https://doi.org/10.1097/AJP.0000000000000123 (2015).

85. Peolsson, A., Ludvigsson, M. L., Overmeer, T., Dedering, A., Bernfort, L., Johansson, G. & et. al. Effects of neck-specific exercise with or without a behavioural approach in addition to precribed physical activity for individuals with chronic whplash-associated disorders: a prospective randomised study. *BMC musculoskeletal disorders.* 14:311. https://doi.org/10.1186/1471-2474-14-311 (2013).

86. Miettinen, T., Leino, E., Airaksinen, O. & Lindgren, K. The possibility to use simple validated questionnaires to predict long-term health problems after whiplash injury. *Spine.* 29:E47-E51 (2004).

87. Harms-Ringdahl, K., Carlsson, A., Ekholm, J., Raustorp, A., Svensson, T. & Toresson, H.-G. Pain assessment with different intensity scales in response to loading of joint structures. *Pain.* https://doi.org/10.1016/0304-3959(86)90163-6 (1986).

88. Giambini, H., Hatta, T., Krzysztof, R. G., Widholm, P., Karlsson, A., Dahlqvist Leinhard, O., Adkins, M. C., Zhao, C. & An, K.-N. Intramuscular fat infiltration evaluated by magnetic resonance imaging predicts the extensibility of the supraspinatus muscle. *Muscle & Nerve* (2018).

89. Mandić, M., Rullman, E., Widholm, P., Lilja, M., Leinhard, O. D., Gustafsson, T. & Lundberg, T. R. Automated assessment of regional muscle volume and hypertrophy using MRI. *Scientific Reports.* https://doi.org/10.1038/s41598-020-59267-x (2020).

90. West, J., Leinhard, O. D., Romu, T., Collins, R., Garratt, S., Bell, J. D., Borga, M. & Thomas, L. Feasibility of MR-Based Body Composition Analysis in Large Scale Population Studies. *PLoS ONE.* https://doi.org/10.1371/journal.pone.0163332 (2016).

91. Ulbrich, E. J., Nanz, D., Leinhard, O. D., Marcon, M. & Fischer, M. A. Whole-body adipose tissue and lean muscle volumes and their distribution across gender and age: MR-derived normative values in a normal-weight Swiss population. *Journal of Magnetic Resonance in Medicine.* 4(10):739-47. https://doi.org/10.1002/mrm.26676 (2017).

92. Linge, J., Borga, M., West, J., Tuthill, T., Miller, M. R., Dumitriu, A., Thomas, E. L., Romu, T., Tunón, P., Bell, J. D. & Leinhard, O. D. Body Composition Profiling in the UK Biobank Imaging Study. *Obesity.* https://doi.org/10.1002/oby.22210 (2018).

93. Machann, J., Bachmann, O., Brechtel, K., Dahl, D., Wietek, B., Klumpp, B., Häring, H. U., Claussen, C. D., Jacob, S. & Schick, F. Lipid content in the musculature of the lower leg assessed by fat selective MRI: intra- and interindividual differences and correlation with anthropometric and metabolic data. *Journal of Magnetic Resonance Imaging.* https://doi.org/10.1002/jmri.10255 (2003).

94. Yoshiko, A., Hioki, M., Kanehira, N., Shimaoka, K., Koike, T., Sakakibara, H., Oshida, Y. & Akima, H. Three-dimensional comparison of intramuscular fat content between young and old adults. *BMC Med Imaging.* https://doi.org/10.1186/s12880-017-0185-9 (2017).

95. Crawford, R. J., Cornwall, J., Abbott, R. & Elliott, J. M. Manually defining regions of interest when quantifying paravertebral muscles fatty infiltration from axial magnetic resonance imaging: a proposed method for the lumbar spine with anatomical cross-reference. *BMC Musculoskeletal Disorders.* https://doi.org/10.1186/s12891-016-1378-z (2017).

96. Elliott, J. M., Cornwall, J., Kennedy, E., Abbott, R. & Crawford, R. J. Content not quantity is a better measure of muscle degeneration in whiplash. *BMC Musculoskeletal Disorders.* https://doi.org/10.1186/s12891-018-2074-y (2018).

97. Peolsson, A., Karlsson, A., Ghafouri, B., Ebbers, T., Engström, M., Jönsson, M., Wåhlén, K., Romu, T., Borga, M., Kristjansson, E., Bahat, H. S., German, D., Zsigmond, P. & Peterson, G. Pathophysiology behind prolonged whiplash associated disorders: study protocol for an experimental study. *BMC musculoskeletal disorders.* 14:311. `https://doi.org/10.1186/s12891-019-2433-3` (2019).

98. Weber, K. A., Smith, A. C., Wasielewski, M., Eghtesad, K., Upadhyayula, P. A., Wintermark, M., Hastie, T. J., Parrish, T. B., Mackey, S. & Elliott, J. M. Deep Learning Convolutional Neural Networks for the Automatic Quantification of Muscle Fat Infiltration Following Whiplash Injury. *Scientific Reports.* `https://doi.org/10.1038/s41598-019-44416-8` (2019).

99. Karlsson, A., Rosander, J., Romu, T., Tallberg, J., Grönqvist, A., Borga, M. & Dahlqvist Leinhard, O. Automatic and Quantitative Assessment of Regional Muscle Volume by Multi-Atlas Segmentation Using Whole-Body Water-Fat MRI. *Journal of Magnetic Resonance Imaging* (2015).

100. Karlsson, A., Dahlqvist Leinhard, O., Åslund, U., West, J., Romu, T., Smedby, Ö., Zsigmond, P. & Peolsson, A. An Investigation of Fat Infiltration of the Multifidus Muscle in Patients with Severe Neck Symptoms Associated with Chronic Whiplash-Associated Disorders. *Journal of Orthopaedic and Sports Physical Therapy* (2016).

101. Karlsson, A., Peolsson, A., Elliott, J., Romu, T., Ljunggren, H., Borga, M. & Dahlqvist Leinhard, O. The Relation Between Local and Distal Muscle Fat Infiltration in Chronic Whiplash Using Magnetic Resonance Imaging. *PLoS ONE* (2019).

102. Karlsson, A., Peolsson, A., Romu, T., Dahlqvist Leinhard, O., Spetz Holm, A.-C., Thorell, S., West, J. & Borga, M. The Effect of Increased Flip Angle when Estimating Muscle Fat Infiltration Using Fat-Referenced Chemical Shift Encoded Imaging. *Submitted for journal publication* (2020).

Papers

The papers associated with this thesis have been removed for copyright reasons. For more details about these see:

http://urn.kb.se/resolve?urn=urn:nbn:se:liu:diva-163501

FACULTY OF SCIENCE AND ENGINEERING

Linköping Studies in Science and Technology, Dissertation No. 2057, 2020
Department of Biomedical Engineering

Linköping University
SE-581 83 Linköping, Sweden

www.liu.se